



**HAL**  
open science

# Mapping The Co2 Total Column Retrieval Performance From Shortwave Infrared Measurements: Synthetic Impacts Of The Spectral Resolution, Signal-To-Noise Ratio, And Spectral Band Selection

Matthieu Dogniaux, Cyril Crevoisier

► **To cite this version:**

Matthieu Dogniaux, Cyril Crevoisier. Mapping The Co2 Total Column Retrieval Performance From Shortwave Infrared Measurements: Synthetic Impacts Of The Spectral Resolution, Signal-To-Noise Ratio, And Spectral Band Selection. Atmospheric Measurement Techniques, 2024, 17, pp.5373-5396. 10.5194/amt-17-5373-2024 . insu-04729837

**HAL Id: insu-04729837**

**<https://insu.hal.science/insu-04729837v1>**

Submitted on 10 Oct 2024

**HAL** is a multi-disciplinary open access archive for the deposit and dissemination of scientific research documents, whether they are published or not. The documents may come from teaching and research institutions in France or abroad, or from public or private research centers.

L'archive ouverte pluridisciplinaire **HAL**, est destinée au dépôt et à la diffusion de documents scientifiques de niveau recherche, publiés ou non, émanant des établissements d'enseignement et de recherche français ou étrangers, des laboratoires publics ou privés.



Distributed under a Creative Commons Attribution 4.0 International License



# Mapping the CO<sub>2</sub> total column retrieval performance from shortwave infrared measurements: synthetic impacts of the spectral resolution, signal-to-noise ratio, and spectral band selection

Matthieu Dogniaux<sup>1,a</sup> and Cyril Crevoisier<sup>1</sup>

<sup>1</sup>Laboratoire de Météorologie Dynamique/IPSL, CNRS, École polytechnique, Institut Polytechnique de Paris, Sorbonne Université, École Normale Supérieure, PSL University, 91120 Palaiseau, France

<sup>a</sup>now at: SRON Netherlands Institute for Space Research, Leiden, the Netherlands

**Correspondence:** Matthieu Dogniaux (m.dogniaux@sron.nl)

Received: 5 November 2023 – Discussion started: 14 November 2023

Revised: 9 June 2024 – Accepted: 20 June 2024 – Published: 12 September 2024

**Abstract.** Satellites have been providing spaceborne observations of the total column of CO<sub>2</sub> (denoted  $X_{\text{CO}_2}$ ) for over two decades now, and, with the need for independent verification of Paris Agreement objectives, many new satellite concepts are currently planned or being studied to complement or extend the instruments that already exist. Depending on whether they are targeting natural and/or anthropogenic fluxes of CO<sub>2</sub>, the designs of these future concepts vary greatly. The characteristics of their shortwave infrared (SWIR) observations notably explore several orders of magnitude in spectral resolution (from  $\lambda/\Delta\lambda \sim 400$  for Carbon Mapper to  $\lambda/\Delta\lambda \sim 25\,000$  for MicroCarb) and include different selections of spectral bands (from one to four bands, among which there are the CO<sub>2</sub>-sensitive 1.6  $\mu\text{m}$  and/or 2.05  $\mu\text{m}$  bands). The very nature of the spaceborne measurements is also explored: for instance, the NanoCarb imaging concept proposes to measure CO<sub>2</sub>-sensitive truncated interferograms, instead of infrared spectra like other concepts, in order to significantly reduce the instrument size. This study synthetically explores the impact of three different design parameters on the  $X_{\text{CO}_2}$  retrieval performance obtained through optimal estimation: (1) the spectral resolution, (2) the signal-to-noise ratio (SNR) and (3) the spectral band selection. Similar performance assessments are completed for the exactly defined OCO-2, MicroCarb, Copernicus CO<sub>2</sub> Monitoring (CO<sub>2</sub>M) and NanoCarb concepts. We show that improving the SNR is more efficient than improving the spectral resolution to increase  $X_{\text{CO}_2}$  precision when

perturbing these parameters across 2 orders of magnitude, and we find that a low SNR and/or a low spectral resolution yield  $X_{\text{CO}_2}$  with vertical sensitivities that give more weight to atmospheric layers close to the surface. The exploration of various spectral band combinations illustrates, especially for lower spectral resolutions, how including an O<sub>2</sub>-sensitive band helps to increase the optical path length information and how the 2.05  $\mu\text{m}$  CO<sub>2</sub>-sensitive band contains more geophysical information than the 1.6  $\mu\text{m}$  band. With very different characteristics, MicroCarb shows a CO<sub>2</sub> information content that is only slightly higher than that of CO<sub>2</sub>M, which translates into  $X_{\text{CO}_2}$  random errors that are lower by a factor ranging from 1.1 to 1.9, depending on the observational situation. The performance of NanoCarb for a single pixel of its imager is comparable to those of concepts that measure spectra at low SNR and low spectral resolution, but, as this novel concept would observe a given target several times during a single overpass, its performance improves when combining all the observations. Overall, the broad range of results obtained through this synthetic  $X_{\text{CO}_2}$  performance mapping hint at the future intercomparison challenges that the wide variety of upcoming CO<sub>2</sub>-observing concepts will pose.

## 1 Introduction

Anthropogenic emissions of carbon dioxide ( $\text{CO}_2$ ) are the main driver of climate change (IPCC, 2021). The current understanding of the global carbon cycle is based on comparisons of results from bottom-up methods, which explicitly model  $\text{CO}_2$ -emitting and  $\text{CO}_2$ -absorbing mechanisms, with those from top-down approaches, which rely on a set of  $\text{CO}_2$  atmospheric concentration observations to find the  $\text{CO}_2$  fluxes that best fit those observations (Friedlingstein et al., 2022). This last approach, called inverse atmospheric transport (Ciais et al., 2010), can ingest in situ observations and/or spaceborne remote estimations of the  $\text{CO}_2$  atmospheric concentration. The latter are produced through inverse radiative transfer, which finds the atmospheric states (including the  $\text{CO}_2$  concentration) that best fit infrared satellite measurements made from space.

Shortwave infrared (SWIR) satellite measurements, which are sensitive to – among others –  $\text{CO}_2$  concentration close to the surface, where fluxes take place, have been exploited for two decades to retrieve the column-averaged dry-air mole fraction of  $\text{CO}_2$  (also called the “total column” and denoted  $X_{\text{CO}_2}$ ). The pioneering ESA Scanning Imaging Absorption Spectrometer for Atmospheric Cartography (SCIAMACHY) instrument (Bovensmann et al., 1999) was the first to provide a global  $X_{\text{CO}_2}$  dataset. Its mission ended in 2012, and it was followed by the – still flying – JAXA/NIES Greenhouse gases Observing SATellites (GOSAT and GOSAT-2; Inoue et al., 2016; Noël et al., 2021; Taylor et al., 2022), the NASA Orbiting Carbon Observatory-2 (OCO-2) and OCO-3 (Taylor et al., 2023), and the Chinese TanSat (Yang et al., 2020). The global  $X_{\text{CO}_2}$  datasets produced by these missions have found applications for the study of natural carbon fluxes at a global scale (e.g. Chevallier et al., 2019; Peiro et al., 2022) and also (even though it was not their primary objective) for the monitoring of point-source anthropogenic emissions (Nassar et al., 2021; Reuter et al., 2019; Zheng et al., 2020).

These different missions will be followed by various concepts that are already planned or still being studied. First, the planned Centre national d'études spatiales (CNES) MicroCarb mission (Bertaux et al., 2020; Pascal et al., 2017) is quite similar to OCO-2 regarding its observation strategy (in terms of its spatial and spectral resolution, as shown in Table 1, although it includes an extra  $\text{O}_2$ -sensitive band) and mainly aims to provide information on natural  $\text{CO}_2$  fluxes. The 2015 Paris Agreement and the 5-year global stocktake system it set up have put in motion a global ambition for spaceborne monitoring of anthropogenic greenhouse gas emissions (mainly  $\text{CO}_2$  and methane, but the latter is not the focus of this work). Indeed, urban areas, which account for 0.5 % of the ice-free continental surface (Liu et al., 2020; Lwasa et al., 2022), are responsible for 70 % of all fossil-fuel-related emissions (Duren and Miller, 2012). In favourable meteorological conditions,  $\text{CO}_2$  plumes arise

from either hotspots, such as megacities, or point sources, such as coal-fired power plants (Kuhlmann et al., 2019). Those plumes may then be observed with spaceborne SWIR imagers, depending on their precision and spatial resolution, and the emission rate associated with the imaged plume can then be inferred either with plume analysis and/or mass-balance approaches (Bovensmann et al., 2010; Varon et al., 2018) or within more usual atmospheric inversion schemes (Broquet et al., 2018; Pillai et al., 2016). Because an infrared detector has a limited number of pixels, future – planned or studied –  $\text{CO}_2$ -imaging concepts explore various trade-offs between the spatial and spectral resolution and spectral band selection, and they even compromise in terms of the very nature of the measurements made by the instrument when other constraints such as size (and thus costs) are taken into consideration. These concepts include – among others – the European Copernicus  $\text{CO}_2$  Monitoring ( $\text{CO}_2\text{M}$ ; Meijer and Earth and Mission Science Division, 2020) mission, the Japanese Global Observing SATellite for Greenhouse gases and Water cycle (GOSAT-GW; Matsunaga and Tanimoto, 2022), the American non-profit Carbon Mapper initiative (<https://carbonmapper.org/>, last access: 17 August 2024) based on the Next-Generation NASA Airborne Visible/Infrared Imaging Spectrometer (Cusworth et al., 2021; Hamlin et al., 2011), the German  $\text{CO}_2\text{Image}$  concept (Strandgren et al., 2020; Wilzewski et al., 2020) and the European Space CARBOn Observatory (SCARBO) H2020 concept, which does not measure spectra, only truncated interferograms (Brooker, 2018; Dogniaux et al., 2022; Gousset et al., 2019). Table 1 gathers the characteristics of upcoming or studied SWIR  $\text{CO}_2$ -observing satellite concepts, which are provided either in scientific articles (in which case citations are provided), in conference presentations (in which case just the conference name and dates are given) or on websites (in which case just the hyperlink is given), as some of these concepts are quite recent.

The characteristics of an observing concept (nature of measurement, spectral resolution, spectral band selection and signal-to-noise ratio) translate into an  $X_{\text{CO}_2}$  retrieval performance that comprises (1) the random error, (2) the systematic error and (3) the vertical sensitivity. First, the  $X_{\text{CO}_2}$  random error (or precision) impacts the a posteriori uncertainties of fluxes estimated in usual inverse atmospheric schemes (Rayner and O'Brien, 2001) and the detectability of  $\text{CO}_2$  plumes for imaging concepts (Kuhlmann et al., 2019). In addition to random errors, systematic errors can hamper  $X_{\text{CO}_2}$  retrievals. Those can, for example, be due to forward radiative transfer modelling errors, like aerosol misknowledge (Houweling et al., 2005; Reuter et al., 2010), or the a priori misknowledge of atmospheric state parameters (Connor et al., 2008). Spatially correlated systematic errors are especially detrimental in inverse atmospheric schemes (Broquet et al., 2018; Chevallier et al., 2007), whereas scene-wide systematic errors that do not correlate with the plume shape can cancel out when applying plume analysis techniques. Fi-

**Table 1.** Measurement characteristics for some of the upcoming or studied SWIR  $\text{CO}_2$ -observing satellite concepts.

Concept	Spatial resolution/swath	Spectral bands	Resolving power ( $\lambda/\Delta\lambda$ )	Reference
OCO-2	1.3 km $\times$ 2.3 km/10 km	O <sub>2</sub> : 0.76 $\mu\text{m}$ CO <sub>2</sub> : 1.6 $\mu\text{m}$ CO <sub>2</sub> : 2.05 $\mu\text{m}$	$\sim$ 18 000 $\sim$ 19 800 $\sim$ 19 800	Crisp et al. (2017)
MicroCarb	4.5 km $\times$ 8.9 km/13.5 km	O <sub>2</sub> : 0.76 $\mu\text{m}$ CO <sub>2</sub> : 1.6 $\mu\text{m}$ CO <sub>2</sub> : 2.05 $\mu\text{m}$ O <sub>2</sub> : 1.27 $\mu\text{m}$	$\sim$ 25 400 $\sim$ 25 750 $\sim$ 25 800 $\sim$ 25 800	Bertaux et al. (2020)
CO <sub>2</sub> M	2 km $\times$ 2 km/ $>$ 250 km	O <sub>2</sub> : 0.76 $\mu\text{m}$ CO <sub>2</sub> , CH <sub>4</sub> : 1.6 $\mu\text{m}$ CO <sub>2</sub> : 2.05 $\mu\text{m}$	$\sim$ 6300 $\sim$ 5400 $\sim$ 5800	Meijer and Earth and Mission Science Division (2020)
GOSAT-GW	3 km $\times$ 3 km/90 km and 10 km $\times$ 10 km/920 km	O <sub>2</sub> : 0.76 $\mu\text{m}$ CO <sub>2</sub> , CH <sub>4</sub> : 1.6 $\mu\text{m}$	$>$ 14 000 $>$ 8000	IWGGMS-17, 14–17 June 2021
CO2Image	50 m $\times$ 50 m/50 km	CO <sub>2</sub> : 2.05 $\mu\text{m}$	$\sim$ 1600	Strandgren et al. (2020)
Carbon Mapper	30 m $\times$ 30 m/18 km	0.4–2.5 $\mu\text{m}$	$\sim$ 400 at $\sim$ 2.05 $\mu\text{m}$	<a href="https://carbonmapper.org/articles/tanager-methane-performance-specifications">https://carbonmapper.org/articles/tanager-methane-performance-specifications</a> (last access: 17 August 2024)
SCARBO	2.3 km $\times$ 2.3 km/195.5 km	Truncated interferograms sensitive to O <sub>2</sub> at 0.76 $\mu\text{m}$ , CO <sub>2</sub> and CH <sub>4</sub> at 1.6 $\mu\text{m}$ , and CO <sub>2</sub> at 2.05 $\mu\text{m}$		Brooker (2018), Dogniaux et al. (2022), Gousset et al. (2019)

nally, the retrieved  $\text{CO}_2$  total columns must be characterized by their vertical sensitivity, which illustrates the atmospheric levels to which retrievals are sensitive (Boesch et al., 2011; Buchwitz et al., 2005).

The impacts of SWIR measurement characteristics on  $X_{\text{CO}_2}$  retrieval performance have been partially examined in previous studies that relied on real measurements. For instance, Galli et al. (2014) assessed the performance of  $X_{\text{CO}_2}$  retrievals from GOSAT measurements for which spectral resolution was degraded by up to 6 times ( $\lambda/\Delta\lambda \sim 3000 - 20000$ ), and Wu et al. (2020) performed a similar exercise with OCO-2 measurements degraded at CO<sub>2</sub>M spectral resolution. Spectral band selection has also been studied: Wu et al. (2019) performed retrievals only using the 2.05  $\mu\text{m}$  band of OCO-2 measurements, and Wilzewski et al. (2020) considered single-band observations from spectrally degraded 1.6  $\mu\text{m}$ /2.05  $\mu\text{m}$  GOSAT band measurements ( $\lambda/\Delta\lambda \sim 700 - 8100/6150$ , respectively).

In this work, we perform a systematic survey that synthetically explores the impact of the spectral resolution, signal-to-noise ratio (SNR) and spectral band selection – three design parameters for SWIR  $\text{CO}_2$ -observing satellite concepts – on  $X_{\text{CO}_2}$  retrieval performance (SNR-related precision, degrees of freedom, vertical sensitivity and smoothing error, with the accuracy excluded). These choices are motivated by the characteristics gathered in Table 1. Indeed, 2 orders of magnitude in resolving power ( $\lambda/\Delta\lambda$ ) separate Carbon Mapper

(AVIRIS-NG) from MicroCarb. Exploring a wide range of SNR values on top of different resolving powers will help to encompass all possible performance results from a wide variety of concepts that measure SWIR spectra. Finally, because CO2Image is planned to measure only the 2.05  $\mu\text{m}$  band and GOSAT-GW will only measure the 0.76 and 1.6  $\mu\text{m}$  bands, we will also study the impact of choosing different combinations of spectral bands. Synthetic calculations performed for a fictitious concept with varying design parameters will help to map a large space of possible  $X_{\text{CO}_2}$  retrieval performances to which those of the peculiar SCARBO concept will be compared, along with those of the current OCO-2 and upcoming MicroCarb and CO<sub>2</sub>M missions.

This article is structured as follows. Section 2 describes the observing concepts considered in this work, and Sect. 3 details the materials and methods. Section 4 describes the results obtained for a fictitious concept with varying design parameters and discusses them. It first focuses on the impact of spectral resolution and SNR, then on the impact of spectral resolution and spectral band selection, for which it also explores geophysical information entanglements. Finally, Sect. 5 discusses the performance results obtained for the exactly defined OCO-2, MicroCarb and CO<sub>2</sub>M concepts, along with those of the peculiar NanoCarb concept, and how they compare to those of the fictitious concept with varying design parameters. Section 6 highlights the conclusions of this work.

## 2 SWIR $\text{CO}_2$ -observing satellite concepts

In this section, we provide the measurement characteristics that are used to model the different upcoming – real or fictitious – SWIR  $\text{CO}_2$ -observing satellite concepts. In order to reduce the number of dimensions to explore, we consider, for the purpose of this study, that the spectra-measuring concepts have identical resolving powers  $\lambda/\Delta\lambda$  across all their spectral bands as well as a constant spectral sampling ratio of 3 (which is the case for both MicroCarb and  $\text{CO}_2\text{M}$  and is a design hypothesis for  $\text{CO}_2\text{Image}$ ). All instrument spectral response functions (ISRFs) are treated as Gaussian functions with a full width at half maximum (FWHM,  $\Delta\lambda$ ) calculated from the resolving power  $\lambda/\Delta\lambda$ , where  $\lambda$  is the average spectral band wavelength.

### 2.1 OCO-2, MicroCarb and $\text{CO}_2\text{M}$

We consider three explicitly described upcoming concepts that measure and will measure SWIR spectra: OCO-2, MicroCarb and the Copernicus  $\text{CO}_2$  Monitoring ( $\text{CO}_2\text{M}$ ) concept. Figure 1a, c, e and g illustrate MicroCarb and  $\text{CO}_2\text{M}$  observations.

The Orbiting Carbon Observatory-2 (OCO-2) has been providing  $X_{\text{CO}_2}$  observations from SWIR measurements for close to a decade (Taylor et al., 2023). We include this instrument in order to assess how the synthetic results obtained here relate to results obtained from real data. Our modelling of OCO-2 observations relies on instrument functions and noise models provided in OCO-2 L1b Science and Standard L2 products of the Atmospheric Carbon Observation from Space algorithm, version 8 (ACOS; O'Dell et al., 2018). These files are not from the latest version (v10) of the OCO-2 data, but the major reprocessing of v8 to v10 did not include significant changes in instrument parameters (Taylor et al., 2023), so we assess that our input data are acceptable for this synthetic study.

MicroCarb (Bertaux et al., 2020; Pascal et al., 2017) is the upcoming CNES  $\text{CO}_2$ -observing mission that will acquire SWIR spectra at high spectral resolution, thus following in the steps of the currently flying OCO-2. Besides the increase in spectral resolution, its main novelty is the addition of the  $\text{O}_2$  1.27  $\mu\text{m}$  band that will provide additional optical path length information at wavelengths closer to those that have  $\text{CO}_2$  sensitivity, which may help to reduce aerosol-related errors. MicroCarb aims at retrieving  $X_{\text{CO}_2}$  with a precision below 1 ppm and with the lowest possible systematic errors. In this work, we use the measurement characteristics presented in Table 2 to model the MicroCarb concept. In Sect. 5, where MicroCarb results are presented, the impact on performance of using both or just one of the  $\text{O}_2$ -sensitive bands will be discussed.

The Copernicus  $\text{CO}_2$  Monitoring ( $\text{CO}_2\text{M}$ ) mission (Meijer and Earth and Mission Science Division, 2020) is the upcoming space component of the operational European anthro-

pogenic  $\text{CO}_2$  emissions Monitoring and Verification Support capacity ( $\text{CO}_2\text{MVS}$ ; Janssens-Maenhout et al., 2020). Its design is a compromise between the spatial and spectral resolutions, the swath and the spectral band width, and it aims to provide imaging of  $X_{\text{CO}_2}$  with a random error lower than 0.7 ppm and systematic errors that are as low as possible (Meijer and Earth and Mission Science Division, 2020). In this work, we use the spectrometer measurement characteristics presented in Table 3 to model the  $\text{CO}_2\text{M}$  concept. Besides the spectrometer, the  $\text{CO}_2\text{M}$  mission will also include a multi-angle polarimeter, which is an instrument dedicated to the observation of aerosols. Its results are expected to help to better constrain their interfering effect on  $X_{\text{CO}_2}$  retrievals and to improve their precision and accuracy (Rusli et al., 2021). Here, we only study the  $\text{CO}_2\text{M}$  spectrometer alone, so the results that we obtain do not reflect the comprehensive theoretical  $\text{CO}_2\text{M}$  mission performance.

### 2.2 The fictitiously varying $\text{CO}_2\text{M}$ concept (CVAR)

In order to grasp the full extent of the upcoming or studied SWIR  $\text{CO}_2$ -observing satellite concepts, we also consider a fictitious concept that has the same characteristics as  $\text{CO}_2\text{M}$  apart from its resolving power  $\lambda/\Delta\lambda$ , SNR and spectral band selection. This varying concept will be hereafter referred to as “CVAR”.

First, we consider resolving-power values ranging from 200 to 30 000 (the list of exact resolving-power values that are considered is given in Table S1 in the Supplement). Figure 2 illustrates the impact of spectral resolution on the  $\text{CO}_2$  absorption band around 1.6  $\mu\text{m}$ . For the lowest resolving power  $\lambda/\Delta\lambda = 200$ , the “two-lobed” P-R branch structure of this  $\text{CO}_2$  absorption band (Liou, 2002) is not visible. It fully appears from  $\lambda/\Delta\lambda = 1000$  upwards. Individual absorption lines become visible but are not fully resolved for  $\lambda/\Delta\lambda$  values between about 1000 and 10 000. Only when  $\lambda/\Delta\lambda > 10 000$  do the whole P-R band structure and individual absorption lines fully appear. Given that the fixed  $\text{CO}_2\text{M}$  spectral band intervals are quite large compared to those of MicroCarb, the choice of using the  $\text{CO}_2\text{M}$  band intervals for exploring the impact of the resolving power on  $X_{\text{CO}_2}$  retrieval performance is a reasonable compromise between high-resolution instruments that measure narrow spectral bands (e.g. MicroCarb or OCO-2) and low-resolution instruments that measure continuous spectra (e.g. Carbon Mapper, which measures from 0.4 to 2.5  $\mu\text{m}$ ). Thus, this compromise yields fictitiously large spectral bands for CVAR cases with high resolving-power values and corresponds to a window selection approach for observations with low spectral resolution, similar to what is actually done to process AVIRIS-NG measurements (Cusworth et al., 2021).

In addition to the spectral resolution, we also consider the impact of the SNR in this study. This will help us to explore the performance of a wider range of SWIR  $\text{CO}_2$ -observing satellite concepts. We will cover 2 orders of magnitude in the

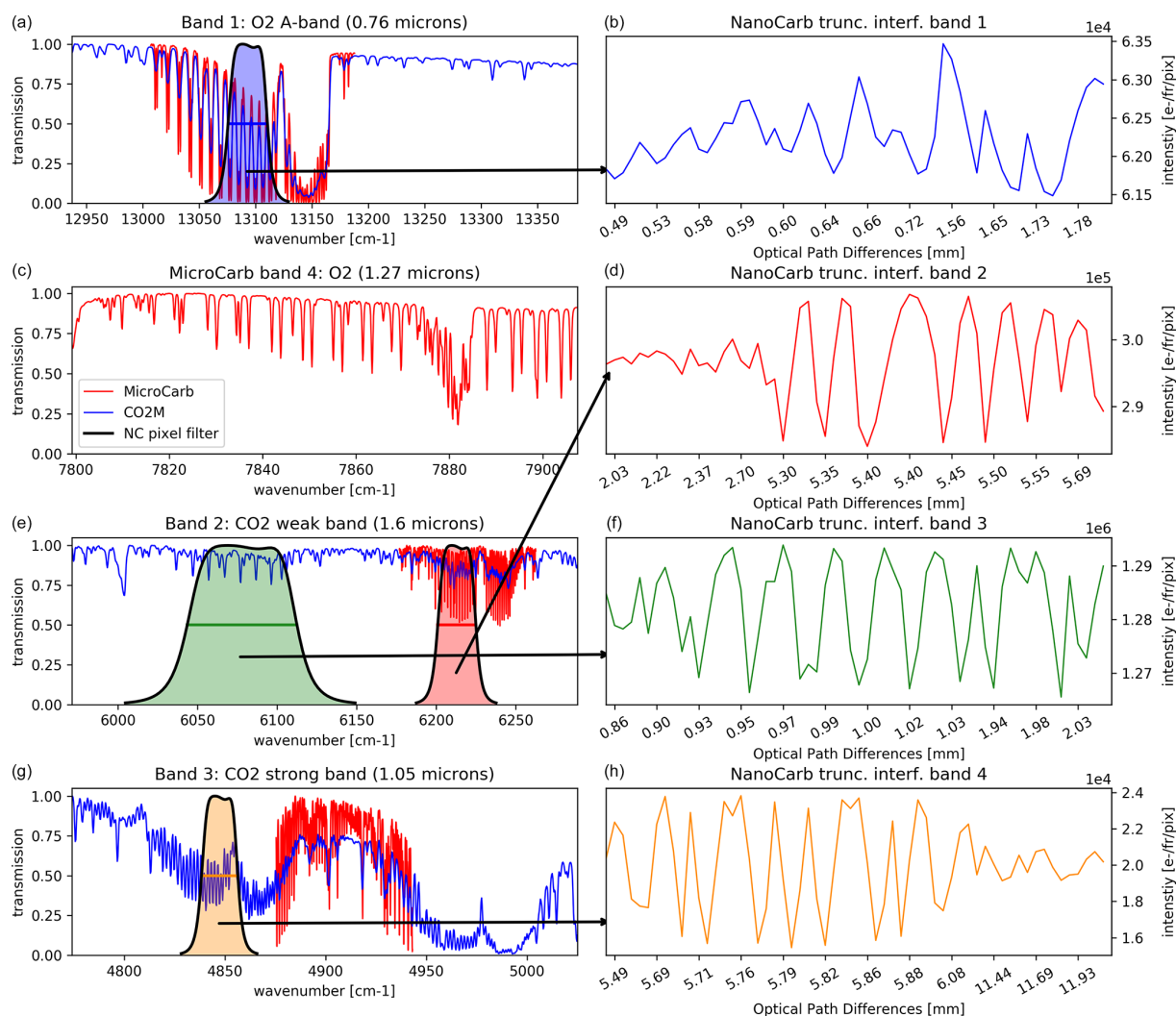


**Figure 1.** Examples of  $\text{CO}_2\text{M}$  (blue) and MicroCarb (red) transmissions (a, c, e, g) and NanoCarb truncated interferograms (in photo-electron per frame per pixel; b, d, f, h) for a vegetation-like albedo with a solar zenith angle of  $50^\circ$ . Arrows link NanoCarb bands to their respective narrowband filters (the horizontal coloured lines denote their FWHMs), which are shown on top of the  $\text{CO}_2\text{M}$  and MicroCarb transmissions.

**Table 2.** MicroCarb measurement characteristics used in this work.

Spectral band	1 ( $\text{O}_2$ A-band)	2 (weak $\text{CO}_2$ band)	3 (strong $\text{CO}_2$ band)	4 ( $\text{O}_2$ 1.27 $\mu\text{m}$ band)
Wavelengths ( $\mu\text{m}$ )	0.758–0.769	1.597–1.619	2.023–2.051	1.265–1.282
Resolving power ( $\lambda/\Delta\lambda$ )	25 000	25 000	25 000	25 000
Spectral sampling ratio	3	3	3	3
Reference radiance $L_{\text{ref}}$ ( $\text{W m}^{-2} \text{cm sr}^{-1}$ )	$4.38 \times 10^{-3}$	$2.69 \times 10^{-3}$	$9.95 \times 10^{-4}$	$2.97 \times 10^{-3}$
Reference SNR ( $\text{SNR}_{\text{ref}}$ )	480	579	249	503

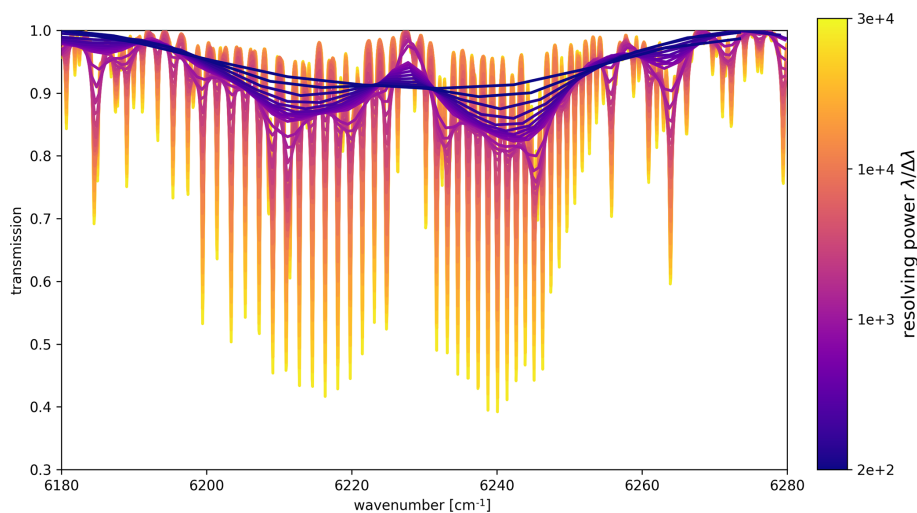
noise level by applying a spectral-band-specific factor ranging from 0.1 to 10 to the  $\text{CO}_2\text{M}$  SNR values given in Table 3. The impacts of both the spectral resolution and SNR on  $X_{\text{CO}_2}$  retrieval performance results are presented and discussed in Sect. 4.1.

Finally, in addition to the spectral resolution but separately from the SNR, we consider the impact of spectral band se-

lection. This will help us to encompass upcoming or studied single- or dual-band observing concepts such as  $\text{CO}_2\text{Image}$  or  $\text{GOSAT-GW}$ , respectively. All  $\text{CO}_2\text{M}$  spectral band combinations containing at least one  $\text{CO}_2$ -sensitive band will be explored: B2, B12, B3, B13, B23 and B123 (B denotes “band” and is followed by the  $\text{CO}_2\text{M}$  spectral band numbers considered in the combination). The impacts of both the

**Table 3.** CO<sub>2</sub>M spectrometer measurement characteristics used in this work.

Spectral band	1 (O <sub>2</sub> A-band)	2 (weak CO <sub>2</sub> band)	3 (strong CO <sub>2</sub> band)
Wavelengths (μm)	0.747–0.773	1.590–1.675	1.990–2.095
Resolving power ( $\lambda/\Delta\lambda$ )	5870	5870	5870
Spectral sampling ratio	3	3	3
Reference radiance $L_{\text{ref}}$ (W m <sup>-2</sup> cm sr <sup>-1</sup> )	$9.66 \times 10^{-4}$	$6.81 \times 10^{-4}$	$7.30 \times 10^{-4}$
Reference SNR (SNR <sub>ref</sub> )	330	400	400

**Figure 2.** CO<sub>2</sub>-sensitive 1.6 μm band observed with a resolving power  $\lambda/\Delta\lambda$  ranging from 200 to 30 000.

spectral resolution and spectral band selection on  $X_{\text{CO}_2}$  retrieval performance results and geophysical information entanglement are presented and discussed in Sect. 4.2.

### 2.3 The SCARBO concept and NanoCarb

The Space CARBOn Observatory (SCARBO) concept (Brooker, 2018) is quite different from all the other concepts mentioned in this article. It relies on a miniaturized static Fabry–Perot interferometer, named NanoCarb, that measures truncated interferograms at optical path differences (OPDs) which are optimally sensitive to CO<sub>2</sub> and to some other interfering geophysical variables (Gousset et al., 2019). Because of their very nature, these truncated interferograms are sensitive to the periodic signature of CO<sub>2</sub> in the infrared spectrum. As in Dogniaux et al. (2022), here we use the latest design of the NanoCarb instrument, currently considered with an  $\sim 200$  km swath and a  $2.3 \text{ km} \times 2.3 \text{ km}$  spatial resolution. The optimal OPD selection accounts for CO<sub>2</sub> information entanglements with H<sub>2</sub>O and aerosols, neglects the atmospheric temperature, and assumes that albedo is constant across each band (Gousset et al., 2019). It measures truncated interferograms that are sensitive to four spectral bands, as shown in the right panels of Fig. 1, which are associated with the narrowband filters shown in Fig. 1a, c, e and g (follow the arrows). Their FWHMs are 35, 24, 69 and  $18 \text{ cm}^{-1}$  for bands 1

to 4, respectively. NanoCarb has a two-dimensional field of view (FOV; 170 across-track  $\times$  102 along-track pixels in the current design) that observes a fixed location on the ground from different viewing angles as it flies over it. The up to 102  $X_{\text{CO}_2}$  retrievals that can be done for the same location on the ground are then combined to yield only one unique retrieval result with a reduced random error (assuming independent observations). Dogniaux et al. (2022) details the NanoCarb concept performance results and its current shortcomings. One of the main results is that NanoCarb performance decreases close to the FOV edges, so we will only focus here on the central FOV pixel and central along-track row of pixels. It also explains that the CO<sub>2</sub> and interfering geophysical variable information contents are entangled in NanoCarb truncated interferograms. This specific shortcoming will be further detailed in this article.

## 3 Materials and methods

### 3.1 Atmospheric and observational situations

As this study focuses on the impact of instrument design parameters on  $X_{\text{CO}_2}$  retrieval performance, we purposefully limit the number of atmospheric conditions that we include. We consider 12 atmospheric and observational situ-

ations that explore three surface albedo models (soil, vegetation and desert, denoted SOL, VEG and DES, respectively; their average values over the SWIR spectral bands are given in Table S2) generated from the ASTER spectral library (Baldrige et al., 2009) and four solar zenith angles (hereafter SZA, 0, 25, 50 and 70°). A given situation will be referred to by the short name of its albedo model followed by the SZA; e.g. VEG-50° corresponds to the situation where the albedo is representative of vegetation and the SZA is equal to 50°.

For these 12 situations, the measurements are made at nadir (a viewing zenith angle equal to 0°). We use a typically European atmospheric situation (vertical temperature and water vapour profiles), taken as the average of the mid-latitude temperate atmospheric profiles included in the Thermodynamic Initial Guess Retrieval (TIGR) climatology library (Chedin et al., 1985; Chevallier et al., 1998). For this synthetic performance study, we consider a constant vertical  $\text{CO}_2$  concentration profile of 394.95 ppm. The surface pressure is constant and set at 1013 hPa. To mimic possible pollution over the European continent, we include fine-mode aerosols (representative of soot) between 0 and 2 km of altitude and coarse-mode aerosols (representative of minerals) between 2 and 4 km of altitude (this choice is supported by desert dust layers that are transported over Europe, as described by Papayannis et al., 2008).

### 3.2 Performance evaluation with optimal estimation

#### 3.2.1 General aspects

Optimal estimation (Rodgers, 2000) offers an ideal framework for the evaluation of  $X_{\text{CO}_2}$  retrieval performance. It has been extensively described in other publications (e.g. Connor et al., 2008), so only its essential aspects are described in this article. Given a state vector  $\mathbf{x}$  that contains parameters that describe the atmospheric and surface states and a measurement vector  $\mathbf{y}$  that contains the infrared observation made from space by a studied concept, OE enables us to provide the geophysical state that best fits the measurement made from space, thus giving a satisfying solution to the following equation:

$$\mathbf{y} = F(\mathbf{x}) + \boldsymbol{\epsilon}, \quad (1)$$

where  $F$  is the forward radiative transfer model that allows us to simulate spaceborne infrared observations from geophysical state parameters and  $\boldsymbol{\epsilon}$  is the spaceborne measurement uncertainty. Because this inverse problem is ill posed, OE brings in a priori information that helps to better constrain the estimation. This a priori information can be seen as the knowledge of the geophysical state one would have before using the information contained in the spaceborne measurement (e.g. taken from climatologies). It is given in the form of an a priori state vector  $\mathbf{x}_a$ , which is characterized by its

uncertainty, as given in the a priori state covariance matrix  $\mathbf{S}_a$ .

The retrieved geophysical state that best fits the measurement made from space and the a priori information is called the maximum-likelihood a posteriori state and is denoted  $\hat{\mathbf{x}}$ . Its a posteriori covariance matrix, which describes the uncertainty of the retrieved state, is denoted  $\hat{\mathbf{S}}$  and computed using the following equation:

$$\hat{\mathbf{S}} = \left[ \mathbf{S}_a^{-1} + \mathbf{K}^T \mathbf{S}_e^{-1} \mathbf{K} \right]^{-1}, \quad (2)$$

where  $\mathbf{S}_e$  is the a priori covariance matrix of the measurement vector describing measurement/forward modelling uncertainties and  $\mathbf{K}$  is the Jacobian matrix containing the partial derivatives of the measurement with respect to the state vector parameters. Its elements for a usual SWIR spectrum and a corresponding NanoCarb truncated interferogram are illustrated in the Supplement (see Figs. S1 and S2).

Another useful OE result is the averaging kernel matrix, denoted  $\mathbf{A}$ , which describes how the retrieved state  $\hat{\mathbf{x}}$  relates to the true – but unknown – geophysical state:

$$\mathbf{A} = \frac{\partial \hat{\mathbf{x}}}{\partial \mathbf{x}} = \hat{\mathbf{S}} \mathbf{K}^T \mathbf{S}_e^{-1} \mathbf{K}. \quad (3)$$

The diagonal elements of  $\mathbf{A}$  are the state vector elements' degrees of freedom, which provide a measure of the geophysical information obtained from the measurement through the OE process. Degrees of freedom close to 1 highlight a high contribution of the measurement to the estimation of a given state vector parameter, whereas degrees of freedom close to 0 denote a low contribution of the measurement and a high contribution of the a priori information. Finally,  $\mathbf{A}$  also enables the computation of the  $X_{\text{CO}_2}$  averaging kernel, which describes its vertical sensitivity (Connor et al., 2008). It shows the atmospheric layers that the retrieval is the most sensitive to and is essential for characterizing and correctly exploiting the retrieved  $X_{\text{CO}_2}$ .

#### 3.2.2 Forward and inverse setups for performance evaluation

We use the 5AI inverse model (Dogniaux et al., 2021), which relies on the 4A/OP radiative transfer model (Scott and Chédin, 1981), to build the Jacobian matrix  $\mathbf{K}$ . These forward radiative transfer simulations rely on the GEISA 2015 spectroscopic database (Jacquinet-Husson et al., 2016) along with line-mixing effects for  $\text{CO}_2$  (Lamouroux et al., 2015) and collision-induced absorption in the  $\text{O}_2$  0.76  $\mu\text{m}$  band (Tran and Hartmann, 2008). Multiple scattering is taken into account through the coupling of 4A/OP with LIDORT (Spurr, 2002), and the aerosol optical properties are taken from the OPAC library, which uses lognormal size distributions (Hess et al., 1998). For the performance study performed here, we assume that these optical properties, including their spectral dependences, are perfectly known, thus allowing the transfer of information when combining different spectral bands.

**Table 4.** State vector used for the performance evaluation.

Variable name	Length	A priori value	A priori uncertainty ( $1\sigma$ )	Notes
H <sub>2</sub> O scaling factor	1	1.0	0.5	–
CO <sub>2</sub> profile	19 layers	394.95 ppm	Same matrix as ACOS (O'Dell et al., 2018)	–
Surface pressure	1	1013.0 hPa	4.0 hPa	–
Temperature profile shift	1	0 K	5 K	–
Surface albedo (order 0 of albedo model)	1–4 bands	True synthetic value	1.0	4 bands in the MicroCarb B1234 and NanoCarb cases
Surface albedo (order 1 of albedo model)	1–4 bands	True synthetic value	1.0	4 bands in MicroCarb B1234. Not included in the state vector for the NanoCarb case; see Sect. 2.3
Coarse-mode aerosol optical depth (COD)	1 layer	0.02	0.1	–
Fine-mode aerosol optical depth (COD)	1 layer	0.05	0.1	–

Finally, the atmospheric model is discretized into 20 atmospheric layers that bound 19 layers, as done by the ACOS algorithm (O'Dell et al., 2018). Airglow emission, which impacts the MicroCarb 1.27  $\mu\text{m}$  band (Bertaux et al., 2020), is not included here in the 4A/OP simulations.

We include in the state vector all the main geophysical variables that are necessary to model SWIR spaceborne measurements. These are listed in Table 4, along with their a priori values and uncertainties. This selection of state vector parameters is used for all exactly defined concepts (with the small exception of the albedo slope for NanoCarb) and CVAR experiment cases because the goal of this study is to explore the impact of design parameters on performance. Using a similar estimation scheme across all resolving powers helps us achieve this goal. However, we do realize that, in practice, less geophysical elements would be fitted for low-resolving-power observations (e.g. Cusworth et al., 2021). Finally, the measurement noise model that fills the diagonal of  $\mathbf{S}_e$  is calculated, as in Buchwitz et al. (2013), with a reference radiance  $L_{\text{ref}}$  and a reference signal-to-noise ratio  $\text{SNR}_{\text{ref}}$ :

$$\sigma_e = \begin{cases} L_{\text{ref}}/\text{SNR}_{\text{ref}}, & \text{if } L < L_{\text{ref}} \\ L/(\text{SNR}_{\text{ref}}\sqrt{L/L_{\text{ref}}}), & \text{if } L \geq L_{\text{ref}}, \end{cases} \quad (4)$$

where  $\sigma_e$  is the noise model for a given spectral sample and  $L$  is the radiance for a given spectral sample. Here, the matrix  $\mathbf{S}_e$  only includes measurement noise, so the uncertainty (or precision) results obtained from the matrix  $\hat{\mathbf{S}}$  will only be related to measurement noise. In practice, smoothing errors from CO<sub>2</sub> and non-CO<sub>2</sub> state vector parameters add up to the uncertainty (Connor et al., 2008). Finally, the uncertainty evaluated for real data is typically larger than the uncertainty obtained from optimal estimation calculations, as model-related errors (the uncertainty in the albedo spec-

tral dependence, spectroscopy errors, etc.) are also encompassed by such evaluations. For example, at low resolving powers, the complexity of the spectral dependence of surface reflectance can lead to significant errors (e.g. for methane; Ayasse et al., 2018) that will not be accounted for here, and, at high resolving power, real-data uncertainties are evaluated to be twice as large as the theoretical uncertainty for OCO-2 (Eldering et al., 2017).

## 4 Results and discussion for CVAR

### 4.1 Impact of the spectral resolution and signal-to-noise ratio

This subsection explores the combined impact of the spectral resolution and signal-to-noise ratio on  $X_{\text{CO}_2}$  retrieval performance. First, we discuss how the  $X_{\text{CO}_2}$  precision and CO<sub>2</sub>-related degrees of freedom evolve with the spectral resolution and signal-to-noise ratio, and then we examine  $X_{\text{CO}_2}$  vertical sensitivities.

#### 4.1.1 $X_{\text{CO}_2}$ precision and degrees of freedom

Here, we assess the impact of varying the spectral resolution and signal-to-noise ratio. For the atmospheric situation VEG-50°, Fig. 3 shows the  $X_{\text{CO}_2}$  precision (or random error) and degrees of freedom (hereafter DOFs) as a function of both the resolving power  $\lambda/\Delta\lambda$  and the signal-to-noise ratio (SNR) for CVAR and the exact OCO-2, CO<sub>2</sub>M, MicroCarb, and NanoCarb concepts (results for exactly defined concepts are discussed in Sect. 5). The random error is computed from the a posteriori covariance matrix  $\hat{\mathbf{S}}$  given in Eq. (2), and the DOFs correspond to the sum of the CO<sub>2</sub>-related diagonal elements of matrix  $\mathbf{A}$ , given in Eq. (3). As the results (i.e.

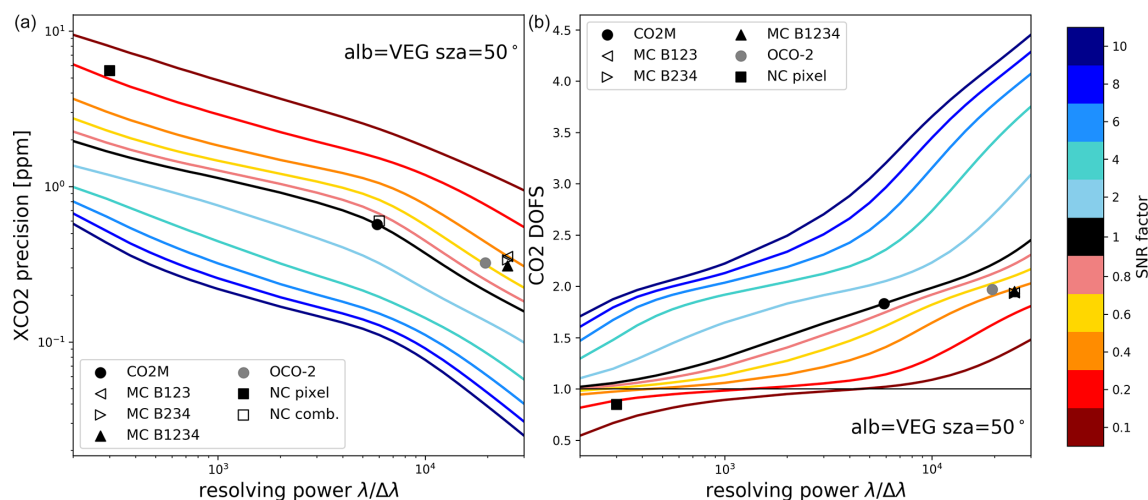


**Figure 3.**  $X_{\text{CO}_2}$  precision (a) and corresponding degrees of freedom for  $\text{CO}_2$  (b) of the fictitious CVAR instrument for a resolving power  $\lambda/\Delta\lambda$  that evolves from 200 to 30 000 (horizontal axis) and for an SNR that evolves from 0.1 to 10 times the  $\text{CO}_2\text{M}$  reference SNR (colour scale) for the situation  $\text{VEG}-50^\circ$ . Symbols give the same quantities for NanoCarb (NC; squares), MicroCarb (MC; triangles for various band combinations),  $\text{CO}_2\text{M}$  (black circles) and  $\text{OCO}-2$  (grey circles). It should be noted that NanoCarb does not have a spectral resolution per se; the resolving powers used to plot its performance were solely chosen for the sake of comparing the performance of NanoCarb and CVAR.

values) change for other albedo models and SZAs but the conclusions do not, figures that include all 12 atmospheric situations are shown in the Supplement.

Results for the reference  $\text{CO}_2\text{M}$  SNR are given by the black line. The  $X_{\text{CO}_2}$  precision evolves from 1.96 ppm for  $\lambda/\Delta\lambda = 200$  to 0.16 ppm for  $\lambda/\Delta\lambda = 30\,000$ . These values are consistent with those reported by previous studies: Galli et al. (2014) showed that degrading the spectral resolution increased the  $X_{\text{CO}_2}$  random errors (values cannot be compared because no real measurement is processed here), and Wu et al. (2020) reported an increase in mean  $X_{\text{CO}_2}$  retrieval noise from 0.25 to 0.59 ppm (compared to an increase from 0.21 to 0.56 ppm in this work) when degrading  $\text{OCO}-2$  measurements ( $\lambda/\Delta\lambda \sim 20\,000$ ) to  $\text{CO}_2\text{M}$ -like resolving powers ( $\lambda/\Delta\lambda \sim 6000$ ). This improvement in precision with increasing resolving power is correlated to DOFS values that also increase with resolving power from 1.02 to 2.45. Indeed, the more information a measurement can bring, the lower the  $X_{\text{CO}_2}$  random error. Changing the SNR has similar effects: the less noisy a measurement, the more information it can carry; thus, increasing the SNR increases the DOFS and reduces the  $X_{\text{CO}_2}$  random error. For example, for  $\lambda/\Delta\lambda = 6000$  (close to the resolution of  $\text{CO}_2\text{M}$ ), the  $X_{\text{CO}_2}$  precision evolves from 2.34 to 0.11 ppm when multiplying the SNR by 100. Overall, increasing the SNR by 2 orders of magnitude improves the  $X_{\text{CO}_2}$  precision by a factor ranging from 16 to 37 (for increasing resolving powers), whereas increasing the resolving power by 2.2 orders of magnitude (from  $\lambda/\Delta\lambda = 200$  to  $\lambda/\Delta\lambda = 30\,000$ ) only improves the  $X_{\text{CO}_2}$  precision by a factor ranging from 10 to 23 (for increasing SNR values). Hence, it appears that the  $X_{\text{CO}_2}$  precision is more sensitive to SNR improvements than

to resolving-power improvements for large improvements of 2 orders of magnitude centred on  $\text{CO}_2\text{M}$  instrument characteristics. However, as it can be seen in Fig. 3 (and in Fig. S3), this conclusion does not hold for smaller local improvements, which generally result in better  $X_{\text{CO}_2}$  precision gains through resolving-power improvements than through SNR improvements (see Fig. S3).

Furthermore, the  $X_{\text{CO}_2}$  precision and DOFS broadly show two slope changes (on a logarithmic scale) as the resolving power  $\lambda/\Delta\lambda$  increases. Depending on the SNR, the first occurs around  $\lambda/\Delta\lambda \sim 400\text{--}1000$ . It corresponds to the complete P-R spectral band structure becoming visible, as previously mentioned in relation to Fig. 2. Then, the second slope change occurs around  $\lambda/\Delta\lambda \sim 4000\text{--}10\,000$ . This corresponds to the individual spectral lines of  $\text{CO}_2$  becoming clearly visible in spectral band branches, as also mentioned in relation to Fig. 2. Between these two slope changes ( $\lambda/\Delta\lambda \sim 1000\text{--}4000$ ), improvements in resolving power are less efficient at improving  $X_{\text{CO}_2}$  precision than they are elsewhere along the resolving-power dimension (see Fig. S3). This explains why, for the large (2 orders of magnitude) improvements in resolving power and SNR explored in this study, the SNR has a larger impact on precision than the resolving power. This result also underlines the critical importance of resolving new spectral features (the P-R band structure below  $\lambda/\Delta\lambda \sim 1000$  or the individual spectral lines above  $\lambda/\Delta\lambda \sim 4000$ ) to gain  $X_{\text{CO}_2}$  precision efficiently.

In addition, we note that these slope changes do not occur at the exact same resolving power for different SNR values, and they vary in sharpness. Indeed, the increase in spectral resolution only brings more information if the band structure and spectral lines, which become progressively visible, are

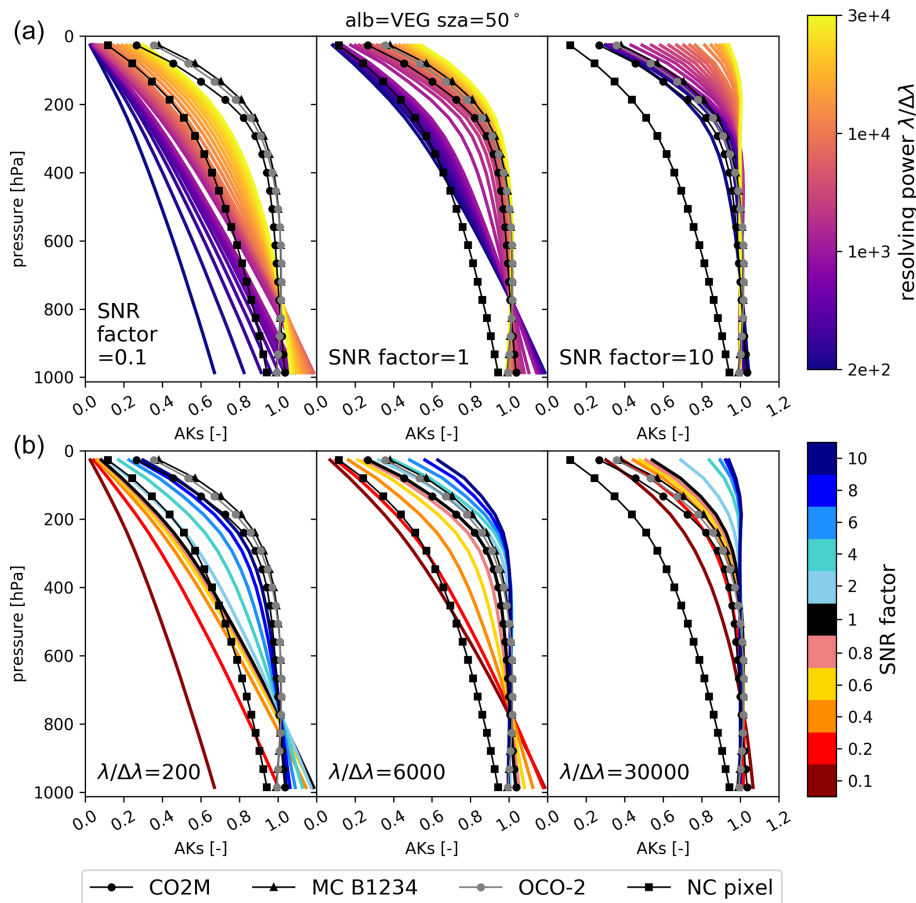


**Figure 4.** Vertical sensitivities (AKs) (a) as a function of resolving power  $\lambda/\Delta\lambda$  for three different SNR scaling factors and (b) as a function of SNR for three different resolving powers  $\lambda/\Delta\lambda$  for the observational situation VEG-50°. Black lines with symbols give the vertical sensitivities for CO<sub>2</sub>M (black circles), MicroCarb (triangles), NanoCarb (squares) and OCO-2 (grey circles).

significant with respect to the noise level. We note that these slope changes occur for smaller resolving powers as SNR increases and that the DOFs and  $X_{\text{CO}_2}$  precision results for a high SNR and low resolving powers correspond to the results for a low SNR and high resolving powers. Thus, there is a broad symmetry in the impact of the SNR and resolving power on  $X_{\text{CO}_2}$  retrieval performance.

#### 4.1.2 Vertical sensitivity: column averaging kernels

In addition to information content (given by the DOFs and, symmetrically, by the precision), the vertical sensitivity (or column averaging kernels, hereafter denoted AKs) of the  $X_{\text{CO}_2}$  retrievals must be examined (see Sect. 3.2.1). Taking into account the vertical sensitivity of total columns is especially important when exploiting local column enhancements of vertically inhomogeneous concentration increases. Indeed, any deviation from unity in the vertical sensitivity wrongfully scales differences between the unknown truth and the prior into the retrieved column enhancement, thus calling for a posteriori corrections, as presented by Krings et

al. (2011) and also included by Borchardt et al. (2021) for aircraft observation processing. Figure 4 shows AKs for CVAR with a resolving power varying from  $\lambda/\Delta\lambda = 200$  to 30 000 and for three different scaling factors of the CO<sub>2</sub>M noise model (top row). It conversely also shows AKs for scaling factors of the CO<sub>2</sub>M noise model that vary from 0.1 to 10 and for three different resolving powers (bottom row). Figure 4 only includes results for the situation VEG-50°. Results for the other situations are shown in the Supplement. For low SNR and resolving-power values, the AKs reach their maximum in the atmospheric layer closest to the ground and have near-zero values at the top of the atmosphere. As the SNR or resolving power (or both) increase, the sensitivities for layers close to the ground improve and become higher than 1. For noise levels and a resolving power of about 6000 and above, the vertical sensitivity values are close to 1 from the ground surface up to approximately 300 hPa and then decrease. For even higher SNR and resolving power layers, the AKs converge towards 1 for all atmospheric layers. Thus, just as for their impact on the  $X_{\text{CO}_2}$  precision or DOFs, the resolving

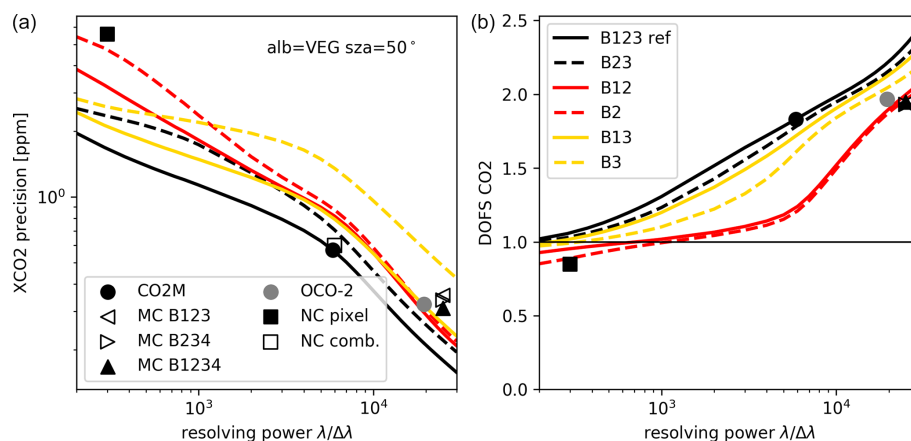


**Figure 5.**  $X_{\text{CO}_2}$  precision (a) and corresponding degrees of freedom for  $\text{CO}_2$  (b) of the fictitious CVAR instrument for a resolving power  $\lambda/\Delta\lambda$  that evolves from 200 to 30 000 (horizontal axis) and for different spectral band selections: with and without the  $\text{O}_2$  0.76  $\mu\text{m}$  band (B1; solid and dashed lines, respectively), with both the  $\text{CO}_2$  1.6 and 2.05  $\mu\text{m}$  bands (B23; black), with only the 1.6  $\mu\text{m}$  band (B2; red), and with only the 2.05  $\mu\text{m}$  band (B3; yellow) for the situation VEG-50°. Symbols give the same quantities for NanoCarb (NC; squares), MicroCarb (MC; triangles for various band combinations),  $\text{CO}_2\text{M}$  (black circles) and OCO-2 (grey circles). It should be noted that NanoCarb does not have a spectral resolution per se; the resolving powers used to plot its performance were solely chosen for the sake of comparing the performance of NanoCarb and CVAR.

power and noise level of an observing concept have very similar impacts on the AK shape for CVAR.

#### 4.2 Impact of spectral resolution and spectral band selection

This subsection explores the combined impact of spectral resolution and band selection on  $X_{\text{CO}_2}$  retrieval performance. First, we discuss how the  $X_{\text{CO}_2}$  precision and  $\text{CO}_2$  and non- $\text{CO}_2$ -related degrees of freedom evolve with spectral resolution and band selection, and then we examine  $X_{\text{CO}_2}$  vertical sensitivities. Finally, we explore the sensitivity of  $X_{\text{CO}_2}$  to a priori misknowledge of interfering geophysical variables, with an eventual focus on aerosol-related parameters.

##### 4.2.1 $X_{\text{CO}_2}$ precision and degrees of freedom for $\text{CO}_2$ and interfering geophysical variables

Here, we assess the impact of varying the spectral resolution and band selection. For the atmospheric situation VEG-50° (results for other situations are given in the Supplement), Fig. 5 shows the  $X_{\text{CO}_2}$  precision and DOFs as a function of both the resolving power  $\lambda/\Delta\lambda$  and spectral band selection for CVAR (with SNR fixed at its reference value) for the exact OCO-2,  $\text{CO}_2\text{M}$ , MicroCarb and NanoCarb concepts (results for exactly defined concepts are discussed in Sect. 5). We first note that including the  $\text{O}_2$  0.76  $\mu\text{m}$  band (denoted B1 in Fig. 5) increases the  $\text{CO}_2$  DOFs for CVAR cases compared to cases where it is not included (denoted B2, B3 and B23 in Fig. 5). This spectral band is indeed sensitive to surface pressure, temperature and aerosols and can thus bring independent constraints on these geophysical parameters that show sensitivities that correlate with the  $\text{CO}_2$  sensitivity of the 1.6

and 2.05  $\mu\text{m}$  bands. For resolving powers above 1000, adding the  $\text{O}_2$  0.76  $\mu\text{m}$  band has less of an impact on the  $X_{\text{CO}_2}$  precision for the B2 than for the B3 cases. This may be explained by the fact that spectral lines are more saturated at B3, so it provides less information regarding the length of the optical path than B2 does. We can also notice that the  $\text{CO}_2$  DOFs for B3 and B13 are always higher than those for the B2 and B12 cases. This may be explained by the fact that the  $\text{CO}_2\text{M}$  2.05  $\mu\text{m}$  band includes two full sets of  $\text{CO}_2$  P-R absorption branches (out of the three present near 2.05  $\mu\text{m}$ , with one more saturated than the other, see Fig. 1), whereas there is only one set of  $\text{CO}_2$  branches in B2 near 1.6  $\mu\text{m}$ , for identical SNR values between B2 and B3. Thus, B3 carries more  $\text{CO}_2$  information than B2. Interestingly, we can also notice that band configurations with higher DOFs do not systematically translate into better  $X_{\text{CO}_2}$  precision: for example, B3 and B13 always show higher DOFs than B2 and B12 but very similar  $X_{\text{CO}_2}$  precisions to them from  $\lambda/\Delta\lambda = 3000$  and upwards. This is due to the covariance between  $\text{CO}_2$  elements in the state vector that vary between band selection cases (see Fig. S18), which shows that different spectral bands carry different  $\text{CO}_2$  information.

For the atmospheric situation VEG-50° (results for other situations are given in the Supplement), Fig. 6 completes Fig. 5 by showing the DOFs for interfering geophysical variables ( $\text{H}_2\text{O}$  profile scaling factor, surface pressure, temperature profile shift and aerosol optical depths; albedo-related parameters are not included because they are all very close or equal to 1) as a function of both the resolving power  $\lambda/\Delta\lambda$  and spectral band selection for CVAR (with the SNR fixed at its reference value) and the exact OCO-2,  $\text{CO}_2\text{M}$ , MicroCarb and NanoCarb concepts (see Sect. 5). For all five vari-

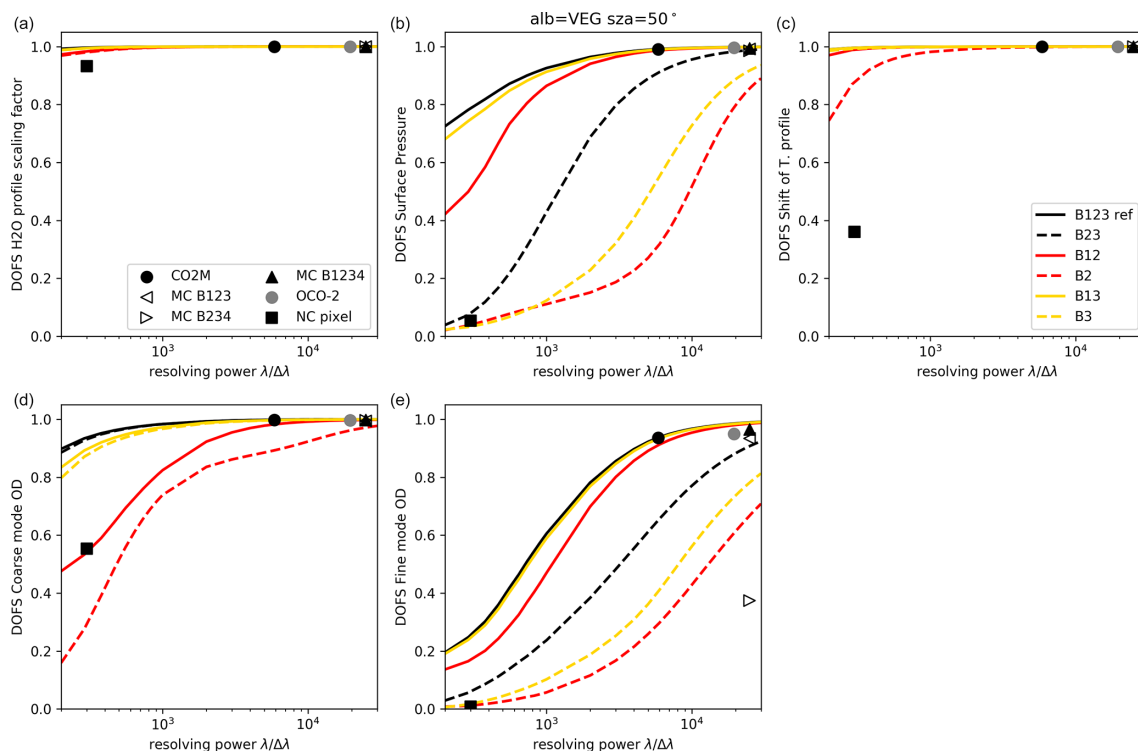


**Figure 6.** Degrees of freedom for the  $\text{H}_2\text{O}$  scaling factor (a), surface pressure (b), temperature profile shift (c), coarse-mode aerosol optical depth (d) and fine-mode aerosol optical depth (e) for the fictitious CVAR instrument with a resolving power  $\lambda/\Delta\lambda$  that evolves from 200 to 30 000 (horizontal axis) and for different spectral band selections: with and without the  $\text{O}_2$   $0.76\ \mu\text{m}$  band (B1; solid and dashed lines, respectively), with both the  $\text{CO}_2$   $1.6$  and  $2.05\ \mu\text{m}$  bands (B23; black), with only the  $1.6\ \mu\text{m}$  band (B2; red), and with only the  $2.05\ \mu\text{m}$  band (B3; yellow) for the situation VEG- $50^\circ$ . Symbols give the same quantities for NanoCarb (NC; squares), MicroCarb (MC; triangles for various band combinations),  $\text{CO}_2\text{M}$  (black circles) and OCO-2 (grey circles). It should be noted that NanoCarb does not have a spectral resolution per se; the resolving powers used to plot its performance were solely chosen for the sake of comparing the performance of NanoCarb and CVAR.

ables, the DOFs increase with resolving power and tend towards 1. The  $\text{H}_2\text{O}$  profile scaling factor and temperature profile shift exhibit high (close to 1) DOFs for almost all resolving powers and spectral band selection cases in the configuration used here. Surface pressure and aerosol optical depths (variables that influence the length of the optical path) have more sensitivity to the resolving power and, especially, to the inclusion – or not – of the  $\text{O}_2$   $0.76\ \mu\text{m}$  band (B1) in the spectral band selection. Cases that do not include B1 show much lower DOFs for these variables, illustrating once again how useful this band is for constraining interfering geophysical variables. This result is made possible by the usual (see the OCO-2 processing algorithm ACOS, for example; O’Dell et al., 2018) hypothesis of fixed aerosol optical properties, which enables the sharing of optical path information across spectral bands. Overall, we can also note that, for all geophysical variables, the DOFs for B13 are more or less significantly closer to those of B123 compared to the DOFs of B12. This shows that the  $\text{CO}_2$   $1.6\ \mu\text{m}$  band brings only a little complementary interfering variable information on the top of that already carried by the  $2.05\ \mu\text{m}$  band.

Previous studies that have explored the impact of spectral band selection and/or the spectral resolution on  $X_{\text{CO}_2}$  performance provide conclusions that are in broad agreement with the previously presented results. Wilzewski et al. (2020) studied the performance of  $X_{\text{CO}_2}$  retrievals from spectrally degraded GOSAT measurements using the  $1.6$  or  $2.05\ \mu\text{m}$  spectral band only. While the methodologies are hardly comparable (because this study is only based on synthetic simulations), both works agree that the trend of  $X_{\text{CO}_2}$  precision against resolving power changes around  $\lambda/\Delta\lambda = 1000$ – $2000$  when solely using the  $1.6$  or  $2.05\ \mu\text{m}$   $\text{CO}_2$  band (see Fig. S11, which shows Fig. 5 plotted on a linear scale). Building on Wilzewski et al. (2020), Strandgren et al. (2020) select the  $2.05\ \mu\text{m}$   $\text{CO}_2$  band for the design of a moderate-resolution instrument, partly because it shows scattering particle sensitivity. The results presented here are consistent with the conclusion that using only the  $2.05\ \mu\text{m}$  band yields higher DOFs (or the same DOFs for surface pressure at low resolving powers) for all geophysical variables compared to when only the  $1.6\ \mu\text{m}$   $\text{CO}_2$  band is used.

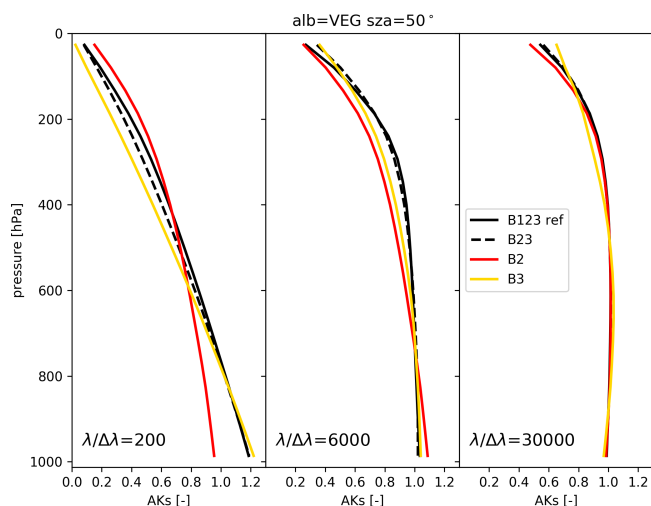


**Figure 7.** Vertical sensitivities (AKs) for different spectral band selections (for explanations of the line colours and styles, see the legend) and three different resolving powers  $\lambda/\Delta\lambda$  for the observational situation VEG-50°.

#### 4.2.2 Vertical sensitivity: column averaging kernels

Figure 7 gives the column averaging kernel – which describes the  $X_{\text{CO}_2}$  vertical sensitivity – for all CVAR spectral band selection cases and for three different resolving-power values (200, 6000 and 30 000). For lower resolving powers, spectral band selection cases that include the  $\text{CO}_2$  2.05  $\mu\text{m}$  band (B3) show a greater sensitivity to atmospheric levels close to the surface. This may be explained by the fact that this spectral band includes saturated spectral lines which are more sensitive to  $\text{CO}_2$  concentration variations in atmospheric layers close to the surface, as it can be seen for example in Fig. 2 in Roche et al. (2021). As seen in Fig. 4, AKs tend to converge towards unity as the resolving power increases, and this difference between bands disappears. Besides, if we compare the AKs for the B23 and B123 spectral band selection cases, we note that including an  $\text{O}_2$ -sensitive band does not have a strong impact on the  $X_{\text{CO}_2}$  vertical sensitivity.

#### 4.2.3 Geophysical information entanglements

Geophysical information is entangled in SWIR measurements (as illustrated for example by the a posteriori correlation matrices shown in Fig. S18 or in Fig. 10) to an extent that depends on the measurement nature (spectrum or truncated interferogram) and its characteristics (spectral band selection, spectral resolution, SNR, etc.). One consequence of these entanglements is that possible a priori misknowledge of the atmospheric state can impact the retrieved  $X_{\text{CO}_2}$  and cause biases; this is called smoothing error (Connor et al., 2008; Rodgers, 2000). In this section, we use the averaging kernel matrix  $\mathbf{A}$  to propagate a priori misknowledge of the synthetic true state of the atmosphere for non- $\text{CO}_2$  interfer-

ing variables in order to evaluate its impact on the retrieved  $X_{\text{CO}_2}$ . Figure 8 shows, for the 12 atmospheric and observational situations considered in this work, the impact on  $X_{\text{CO}_2}$  of a priori misknowledge of several state vector variables for all CVAR spectral band selection cases, for resolving-power values ranging from 200 to 30 000, and for the exact Micro-Carb,  $\text{CO}_2\text{M}$  and NanoCarb concepts (see Sect. 5 for the exactly defined concepts). These a priori perturbations include (1) +10 % to the  $\text{H}_2\text{O}$  profile scaling factor, (2) +1 hPa to the surface pressure, (3) +1 K to the temperature profile shift, and (4) +0.05 to the albedo in the 1.6  $\mu\text{m}$  band. All situations and perturbations are sorted along a unique axis, and Fig. 8a describes both the situations (albedo and SZA) and the perturbations considered.

First, regarding water vapour, the  $X_{\text{CO}_2}$  sensitivity is very small for all CVAR band selection configurations (consistent with the results in Fig. 6), spectral resolutions and exactly described concepts: it amounts to a maximum of 0.12 ppm in absolute value for VEG-70° in the CVAR B3 case for the lowest resolving power. This means that if a water vapour plume is correlated with a  $\text{CO}_2$  emission plume (in the exhaust fumes of a coal-fired power plant, for instance), a small bias in the retrieved  $X_{\text{CO}_2}$  enhancement could then hamper estimations from an instrument with low resolving power (but, potentially, high spatial resolution). However, considering that emission rates computed from enhancements with mass-balance approaches may have uncertainties of up to 65 % (mainly due to wind-speed errors; Varon et al., 2018), this sensitivity of the retrieved  $X_{\text{CO}_2}$  to water vapour appears insignificant.

Regarding surface pressure, the  $X_{\text{CO}_2}$  sensitivities are close to zero for all resolving powers above 10 000 and increase differently depending on the spectral band selection case for lower resolving powers. They reach up to 0.47 ppm for the CVAR B3 case at the lowest resolving-power value tested. Overall, the sensitivity of  $X_{\text{CO}_2}$  to prior surface pressure misknowledge is reduced when the  $\text{O}_2$  0.76  $\mu\text{m}$  band is included in the measurement, consistent with the results shown in Fig. 6. These sensitivities can be expected to impact the full swath of an imaging instrument with lower resolving powers and can thus be removed when computing an enhancement. However, they would blindly impact observations without emission plumes to detect, thus making these observations hard to exploit for other purposes than anthropogenic point-source monitoring.

Regarding the temperature profile global shift, consistent with the high DOFs shown in Fig. 6, the  $X_{\text{CO}_2}$  sensitivities are very small overall for spectral resolving powers above 1000 and for all CVAR spectral band selection cases. For resolving powers lower than 1000, they can reach up to 0.23 ppm in absolute value (for the CVAR B2 case, for instance; see the lower DOFs in Fig. 7).

Finally, all cases and concepts exhibit near-zero  $X_{\text{CO}_2}$  sensitivities (or even, by construction, exactly zero  $X_{\text{CO}_2}$  sensitivities for the CVAR B3 and B13 cases) when the 1.6  $\mu\text{m}$

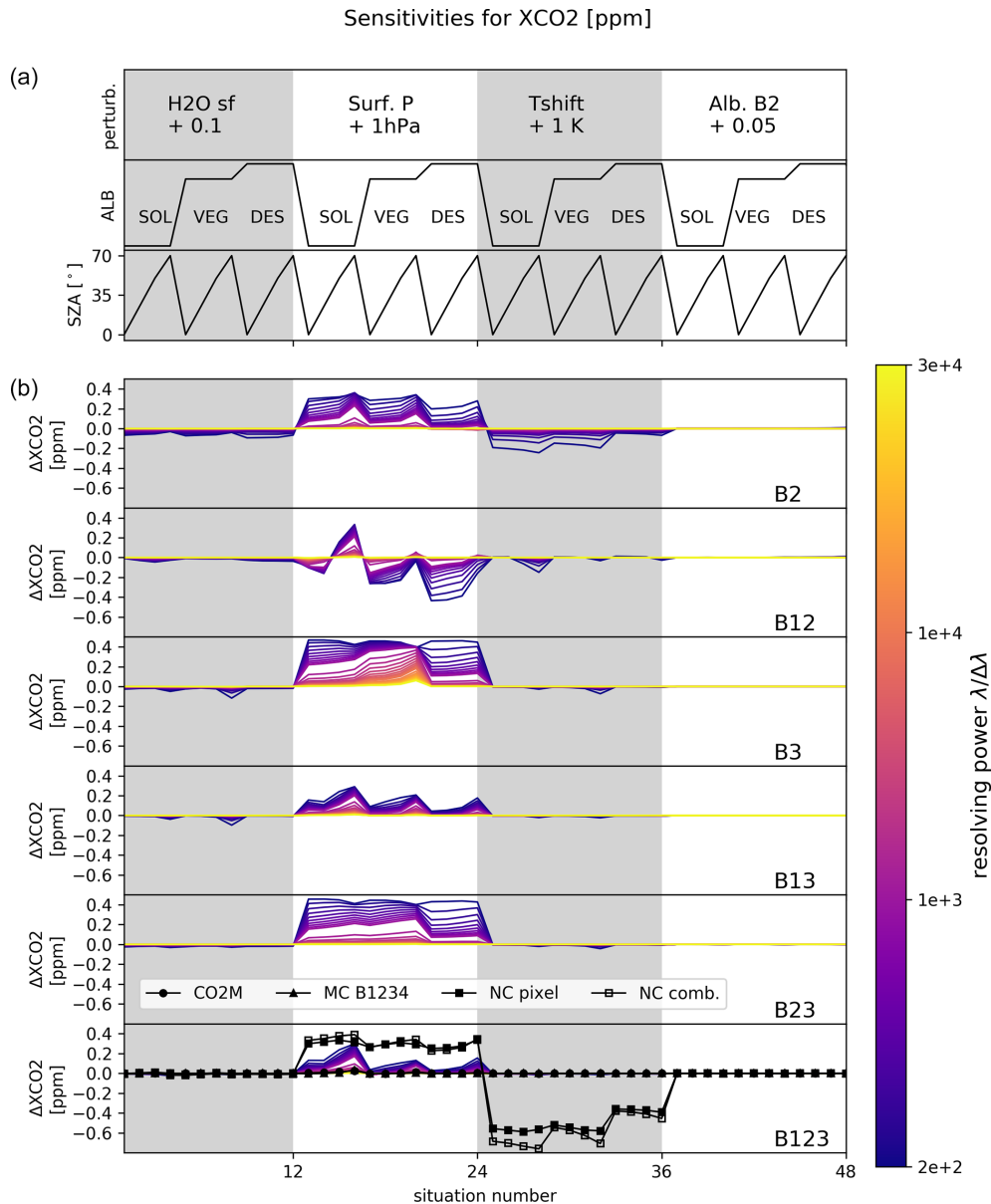


**Figure 8.**  $X_{\text{CO}_2}$  sensitivities (denoted  $\Delta X_{\text{CO}_2}$ ) to prior misknowledge of the water vapour, surface pressure, temperature profile shift and  $1.6 \mu\text{m}$  band albedo value (perturb., described in the top panel) for 12 observational situations (ALB and SZA, described in the second and third panels), six different CVAR spectral band selections (lines in the six bottom panels) and resolving-power values ranging from 200 to 30 000 (colour scale). Black lines with symbols give the same sensitivities for  $\text{CO}_2\text{M}$  (circles), MicroCarb (triangles) and NanoCarb (squares) in the bottom panels (B2, B12, B3, B13, B23 and B123; **b**).

$\text{CO}_2$  band albedo is perturbed by 0.05. This reflects the albedo DOFs (which are very close or equal to 1) that we obtain with this inverse setup configuration as well as the low posterior correlations between albedo and  $\text{CO}_2$  parameters in the state vector.

#### 4.2.4 Focus on sensitivities to prior aerosol misknowledge

We follow the approach used for NanoCarb performance assessment (Dogniaux et al., 2022), which was first introduced by Buchwitz et al. (2013) for the performance assessment of CarbonSat. Considering the 12 previously described atmospheric and observational situations that span three different albedo models and four SZA values, we explore the  $X_{\text{CO}_2}$  sensitivities for synthetic coarse-mode aerosol optical

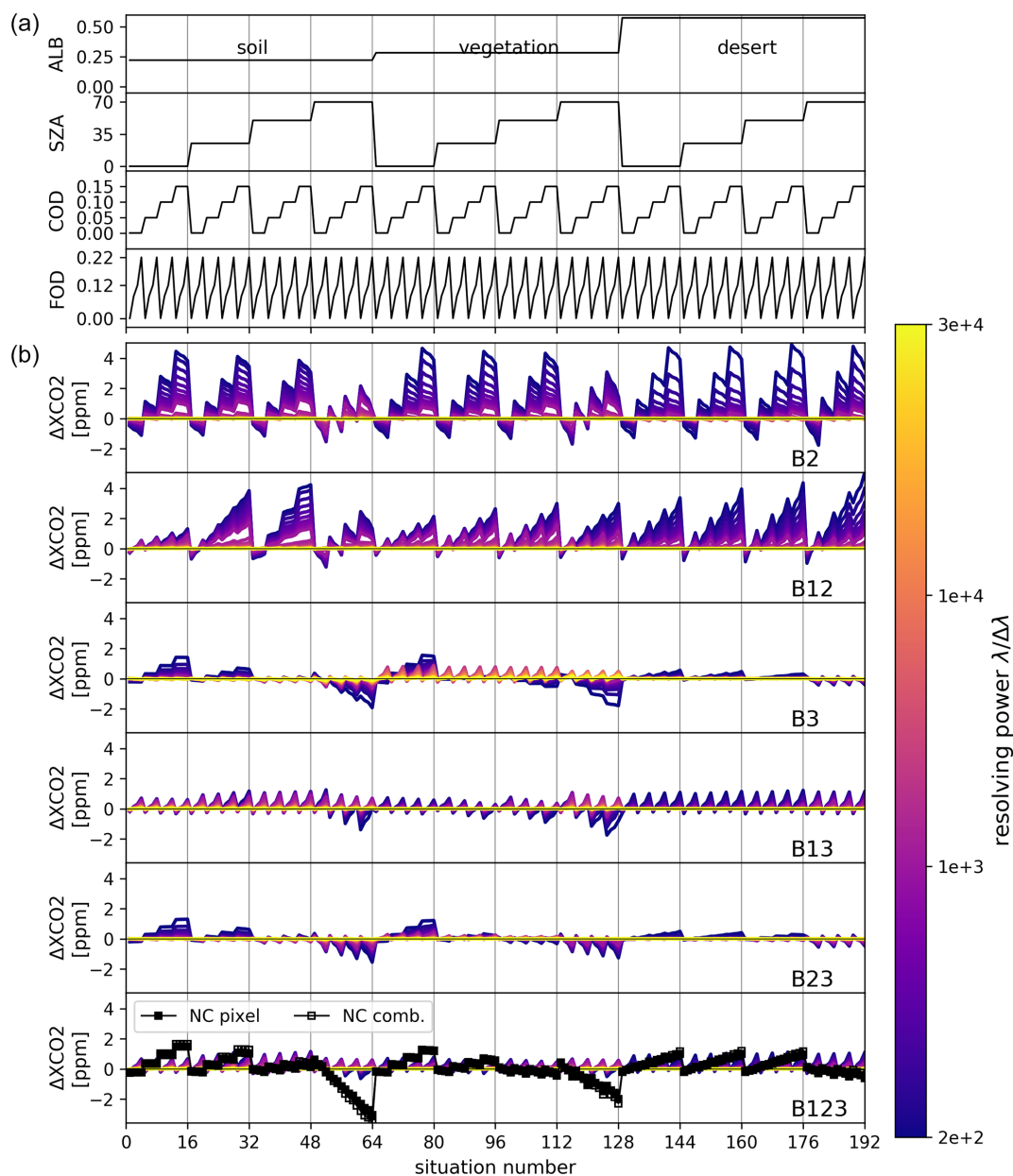


**Figure 9.**  $X_{\text{CO}_2}$  sensitivities (denoted  $\Delta X_{\text{CO}_2}$ ) to prior misknowledge of aerosol optical depths (COD and FOD, described in the third and fourth top panels) for 12 observational situations (ALB and SZA, described in first and second top panels), six different CVAR spectral band selections (B2, B12, B3, B13, B23 and B123; lines in the bottom six panels; **b**) and resolving-power values ranging from 200 to 30 000 (colour scale). Black lines with symbols (squares) in the bottom panel (B123; **b**) give the same sensitivities for NanoCarb (line B123).

depths spanning 0.001–0.15 (with a fixed prior of 0.02) and fine-mode aerosol optical depths spanning 0.001–0.22 (with a fixed prior of 0.05), thus yielding 192 situations in total. This a priori misknowledge of aerosol optical depths is propagated through the averaging kernel matrix  $\mathbf{A}$  to evaluate its impact on retrieved  $X_{\text{CO}_2}$  values.

Figure 9 shows, for the 192 considered situations, the impact of a priori aerosol optical depth misknowledge on  $X_{\text{CO}_2}$  for all CVAR spectral band selection cases, for resolving-

power values ranging from 200 to 30 000, and for the exact NanoCarb concept (results for NanoCarb are discussed in Sect. 5). All situations are sorted along a unique axis, and the top four panels in Fig. 9a (ALB, SZA, COD and FOD) describe the given situation (in terms of albedo, SZA, and coarse- and fine-mode optical depths).

For the CVAR B2 and B12 cases, the  $X_{\text{CO}_2}$  sensitivities at low resolving powers reach up to about  $\sim 5$  ppm. They correlate mostly to a priori misknowledge of the coarse-mode

aerosol optical depth and secondarily to a priori misknowledge of the fine-mode aerosol optical depth, and they diminish as the spectral resolving power increases. Sensitivities also depend on the albedo model and SZA value, thus reflecting that the information content carried by a given measurement also depends on the scene (see the DOFs for all situations in the Supplement). Including the  $\text{O}_2$  0.76  $\mu\text{m}$  band in addition to the  $\text{CO}_2$  1.6  $\mu\text{m}$  band reduces the  $X_{\text{CO}_2}$  sensitivity to a priori aerosol misknowledge at low SZA values for low resolving powers, but it has a low or even a detrimental impact at higher SZAs.

Unlike the  $\text{CO}_2$  1.6  $\mu\text{m}$  band, the  $\text{CO}_2$  2.05  $\mu\text{m}$  band carries more aerosol information, and thus the results for the CVAR B3 and B13 selection cases show lower impacts of these variables on  $X_{\text{CO}_2}$  retrievals, with a maximum of  $\sim 2$  ppm in absolute value. For the CVAR B3 case, the  $X_{\text{CO}_2}$  sensitivities to a priori aerosol misknowledge are mostly correlated to coarse-mode misknowledge for low resolving powers and to fine-mode misknowledge for higher resolving powers, and they converge towards near-zero values for the highest resolving powers. Interestingly, including the  $\text{O}_2$  0.76  $\mu\text{m}$  band changes this correlation pattern, and the  $X_{\text{CO}_2}$  sensitivities appear to be mostly correlated to fine-mode aerosol misknowledge in the B13 case, with slightly higher  $X_{\text{CO}_2}$  sensitivities compared to the B3 case seen in some situations, such as in those with a soil-like or desert-like albedo.

Results for B23 and B123 mostly follow the patterns seen in the B3 and B13 cases (as B3 brings more aerosol information compared to B2) but with slightly lower  $X_{\text{CO}_2}$  sensitivity values, reflecting the scant complementary information added by B2 on top of B3.

## 5 Results and discussion for exactly defined concepts: OCO-2, $\text{CO}_2\text{M}$ , MicroCarb and NanoCarb

### 5.1 $X_{\text{CO}_2}$ precision and degrees of freedom

Besides the results for CVAR, Fig. 3 also includes the performance computed for four explicit concepts: the currently flying OCO-2 and upcoming  $\text{CO}_2\text{M}$  and MicroCarb missions as well as the NanoCarb concept that is currently being studied. First, OCO-2 shows a noise-only-related precision of 0.32 ppm, corresponding to 1.97 DOFs for  $\text{CO}_2$ -related parameters. The OCO-2 results that we obtain are consistent overall with ACOS results for soundings, with close albedo values per band (see Fig. S6). Also, land nadir OCO-2  $X_{\text{CO}_2}$  retrievals show an overall standard deviation of 0.77 ppm compared to the Total Carbon Column Observing Network (TCCON) validation reference (Taylor et al., 2023). This difference with respect to the theoretical uncertainty computed from optimal estimation stems from all the forward and inverse modelling errors that are not accounted for in the retrieval scheme. Thus, this illustrates that the results provided in this study are a lower bound on the actual

precisions that these upcoming concepts will have.  $\text{CO}_2\text{M}$  shows an  $X_{\text{CO}_2}$  precision of 0.56 ppm, which is consistent with the 0.7 ppm precision requirement for a vegetation scene with  $\text{SZA} = 50^\circ$  given in Meijer and Earth and Mission Science Division (2020). For MicroCarb (MC1234 when including the four spectral bands), we find an  $X_{\text{CO}_2}$  precision of 0.31 ppm, which satisfactorily compares to the median 0.35 ppm contribution of the SNR to the mission error budget (with the full range of possible contributions being 0.15–0.94 ppm, Denis Jouglet, personal communication, 2021). Also, we can notice that removing one of the two  $\text{O}_2$ -sensitive spectral bands from MicroCarb measurements (i.e. we consider MC123, which includes the 0.76, 1.6 and 2.05  $\mu\text{m}$  bands, and MC234, which includes the 1.6, 2.05 and 1.27  $\mu\text{m}$  bands) slightly decreases the precision. Indeed, less geophysical information is available to help constrain interfering variables. Finally, MicroCarb (MC1234) shows only slightly higher  $\text{CO}_2$  DOFs compared to  $\text{CO}_2\text{M}$  despite having a spectral resolution that is 5 times higher. This may be explained by the fact that their respective spectral bands do not cover the same wavelength intervals, as can be seen in Fig. 1.

Two different  $X_{\text{CO}_2}$  precision results are included for NanoCarb in Fig. 3: one for a unique pixel located at the FOV centre (filled square) and another obtained after combining results acquired from different viewing angles as the two-dimensional FOV of NanoCarb flies over a scene (see Sect. 2.3 or the extensive description in Dogniaux et al., 2022). For a single observation of a given scene performed by the central pixel in the FOV, NanoCarb yields a precision of 5.6 ppm. However, after combining the maximum number of observations (102, over different viewing angles) of the same scene, the NanoCarb random error is reduced to 0.60 ppm, which is close to the performance of  $\text{CO}_2\text{M}$ . It must be noted that, because of its very nature, NanoCarb does not have a spectral resolution per se. Thus, we arbitrarily attributed a resolving power of  $\lambda/\Delta\lambda = 300$  to plot the pixel-wise performance of NanoCarb and a resolving power of  $\lambda/\Delta\lambda = 6000$  to plot the performance of NanoCarb for combined pixels. This choice enables us to highlight that the pixel-wise performance of NanoCarb is comparable to concepts that measure spectra at low spectral resolution and with low SNR, whereas when the retrieval results from observations that are assumed independent are combined, the  $X_{\text{CO}_2}$  precision becomes comparable to that of  $\text{CO}_2\text{M}$ .

However, despite their similar precisions, further comparisons enable us to show how their respective  $X_{\text{CO}_2}$  observations are not equivalent. Indeed, we first notice that their respective DOFs are not comparable at all:  $\text{CO}_2\text{M}$  shows 1.83 DOFs for  $\text{CO}_2$ , whereas the pixel-wise  $\text{CO}_2$  DOFs of NanoCarb amount to 0.85 (no averaging kernel matrix is computed for the NanoCarb combined-pixel results, as performance is evaluated per pixel and they are assumed to be independent when combined). These low  $\text{CO}_2$  DOFs for NanoCarb are explained by the low  $\text{CO}_2$  information content

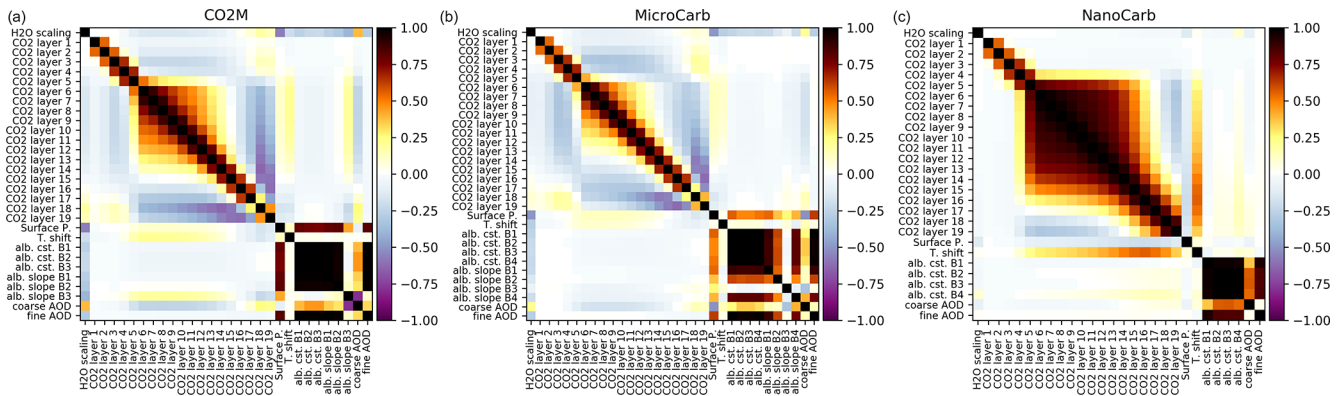


**Figure 10.** A posteriori correlation matrices for CO<sub>2</sub>M (a), MicroCarb (b) and NanoCarb (c) for the VEG-50° situation.

of NanoCarb measurements (compared to concepts that measure spectra) and its entanglement with other geophysical-variable information, as mentioned in Dogniaux et al. (2022). One can indeed notice that the partial derivatives of CO<sub>2</sub> and other variables are correlated (see Fig. S2): this makes it harder for OE to yield independent estimates for CO<sub>2</sub> and other parameters.

Another way to look at this issue is to consider a posteriori correlations between state vector parameters, as given by the a posteriori covariance matrix  $\hat{S}$ . Pearson correlation coefficient matrices computed from  $\hat{S}$  are shown for CO<sub>2</sub>M, MicroCarb (MC1234) and NanoCarb in Fig. 10. First, regarding the CO<sub>2</sub> profile, we notice the very high positive correlation between different atmospheric layers for NanoCarb compared to the CO<sub>2</sub>M and MicroCarb cases. This is a result of the low CO<sub>2</sub> information content in NanoCarb measurements compared to CO<sub>2</sub>M and MicroCarb. Also, in this state vector configuration, the NanoCarb a posteriori covariance matrix shows a stronger correlation between CO<sub>2</sub> atmospheric layers and the temperature profile shift than seen for CO<sub>2</sub>M and MicroCarb. A slight positive correlation between CO<sub>2</sub> atmospheric layers and albedo parameters can also be noted for NanoCarb, unlike for CO<sub>2</sub>M and MicroCarb, which show small negative correlations. The correlation (which has a value of close to 1.0) between albedo parameters of different bands is due to the presence of aerosol optical depth parameters in the state vector (assuming fixed aerosol optical properties). When aerosol optical depths are removed from the state vector, these correlations between albedo parameters of different bands decrease (see Fig. S19). Interestingly, in that case, the correlations between CO<sub>2</sub> atmospheric layers and albedo parameters reach up to 0.6 for NanoCarb, whereas they reach 0.2 and 0.1 for CO<sub>2</sub>M and MicroCarb, respectively (see the Supplement). Thus, all things considered, NanoCarb contains less geophysical information than other concepts that measure spectra, and such a comparison helps pave the way for future improvement of the NanoCarb concept.

## 5.2 Vertical sensitivity: column averaging kernels

Besides the results for CVAR, Fig. 4 also includes the vertical sensitivities of OCO-2, CO<sub>2</sub>M, MicroCarb and NanoCarb. Thanks to their spectral resolutions and SNRs, CO<sub>2</sub>M and MicroCarb show vertical sensitivities that are close to 1 from the surface to about 300 hPa and then decrease. Interestingly, NanoCarb AKs do not have exactly the same shape as the CVAR, CO<sub>2</sub>M or MicroCarb AKs. For the atmospheric layers closest to the ground, the NanoCarb AK follows the AK shape of an instrument with low resolving power and a low SNR (consistent with how the NanoCarb single-pixel performance compares to CVAR in Fig. 3). For higher atmospheric layers, it follows the AK shape of an instrument with medium resolving power and a low SNR or vice versa.

## 5.3 Non-CO<sub>2</sub> degrees of freedom

Besides the results for CVAR, Fig. 6 also gives interfering variable DOFs for the exact OCO-2, CO<sub>2</sub>M, MicroCarb and NanoCarb concepts. For MicroCarb, OCO-2, and CO<sub>2</sub>M, the DOFs for the H<sub>2</sub>O profile scaling factor, surface pressure, temperature global shift and coarse-mode aerosol optical depth are all nearly equal to 1. Only for the fine-mode aerosol optical depth do the DOFs appear to be – slightly – lower than 1, with the exception of the MicroCarb B234 configuration test, where the fine-mode DOF is close to 0.4. This shows that different optical path length information is carried depending on whether the O<sub>2</sub> 0.76 μm or 1.27 μm band is used. NanoCarb exhibits near-zero DOFs for surface pressure and fine-mode optical depth in this retrieval configuration as well as non-zero yet rather low DOF values for H<sub>2</sub>O profile scaling factor, temperature global shift and coarse-mode aerosol optical depth (0.93, 0.36 and 0.55, respectively). Given how small some of these DOF values are, we also conclude that the state vector used to process NanoCarb measurements should be adjusted to only include the most essential geophysical variables. For example, aerosol optical depths could be removed.

#### 5.4 Geophysical information entanglements

Besides the results for CVAR, Fig. 8 also gives the sensitivities of  $\text{CO}_2\text{M}$ , MicroCarb and NanoCarb  $X_{\text{CO}_2}$  to a priori misknowledge of the water vapour, surface pressure, temperature profile, and  $1.6\ \mu\text{m}$  albedo. These  $X_{\text{CO}_2}$  sensitivities are close to zero for MicroCarb and  $\text{CO}_2\text{M}$  for the four tested geophysical variables.

Prior misknowledge of the surface pressure reaches up to 0.39 ppm for NanoCarb, again indicating results comparable to low-spectral-resolution instruments. The sensitivities for the NanoCarb central-pixel results (filled squares) and the NanoCarb combined results for the central row of pixels (empty squares) differ slightly because information entanglement evolves depending on the pixel location in the NanoCarb FOV. NanoCarb also shows significant  $X_{\text{CO}_2}$  sensitivities to a priori temperature misknowledge that reach  $-0.76$  ppm, consistent with the strong correlation shown between the temperature profile shift and  $\text{CO}_2$ -related parameters in the state vector (see Fig. 10). This result is not surprising as the version of the NanoCarb concept used in this work did not consider the possible impact of entanglements between  $\text{CO}_2$  and temperature (see Sect. 2.3 or Dogniaux et al., 2022, Gousset et al., 2019). This paves the way for future improvements of this very compact instrumental concept.

Regarding the sensitivity to prior aerosol misknowledge, Fig. 9 also shows results for the exact NanoCarb concept: those for both the central pixel in the FOV and the combination of the central along-track row of pixels. For SZA values lower than or equal to  $50^\circ$  in soil and vegetation albedo situations and for all SZAs in desert albedo situations, those mostly correlate with the coarse-mode aerosol misknowledge, reaching absolute values of up to 1.7 ppm. For  $\text{SZA} = 70^\circ$  in soil and vegetation albedo situations, not only do the NanoCarb aerosol DOFs increase (see Figs. S16 and S17), but correlations between  $\text{CO}_2$  and aerosol state variables also increase by a lot (see Fig. S20), thus leading to the larger sensitivities shown in Fig. 9 (or Fig. 11). This illustrates that different surface types and SZAs must be explored for thorough performance assessments.

Figure 11 is similar to Fig. 9 but focuses on the exact concepts of  $\text{CO}_2\text{M}$  and MicroCarb studied. Their  $X_{\text{CO}_2}$  sensitivities to prior aerosol optical depth misknowledge are overly correlated to that of fine-mode optical depth. This can be explained by the fact that their coarse-mode optical depth DOFs are very close to 1, thus enabling the correct estimation (in this synthetic simulation setup) of this geophysical parameter, which results in a very low impact of coarse-mode optical depth misknowledge on  $X_{\text{CO}_2}$  retrievals. However, their fine-mode DOFs are below 1, thus leading to estimation errors that impact  $X_{\text{CO}_2}$  retrievals through a posteriori correlations (see Figs. 10 and S19). Overall,  $\text{CO}_2\text{M}$  shows sensitivities of up to 0.2 ppm, with maximums reached for the SOL- $25^\circ$  situation. These values are well below the 0.5 ppm systematic error requirement (Meijer and Earth and Mission Science Di-

vision, 2020) and are expected to be reduced even more by using the aerosol observations provided by the multi-angle polarimeter that will fly alongside the  $\text{CO}_2\text{M}$  spectrometers (Rusli et al., 2021). As for MicroCarb, its  $X_{\text{CO}_2}$  sensitivities to aerosol optical depth misknowledge peak for soil albedo situations at about 0.6 ppm when only the  $0.76\ \mu\text{m}$   $\text{O}_2$  band (B123) is included and at 0.1 ppm when both the  $0.76$  and  $1.27\ \mu\text{m}$   $\text{O}_2$  bands are included (B1234), whereas they peak at  $-0.2$  ppm for vegetation albedo situations when only the  $1.27\ \mu\text{m}$   $\text{O}_2$  band is available (B234). Interestingly, the sensitivities of MicroCarb B123 and B1234 are positively correlated to the fine-mode aerosol optical depth values, whereas those of MicroCarb B234 are negatively correlated. This illustrates that the  $\text{O}_2$   $1.27\ \mu\text{m}$  band carries optical path length information complementary to that carried by the  $\text{O}_2$   $0.76\ \mu\text{m}$  band (see also the a posteriori correlation matrices in Fig. S21).

#### 6 Conclusions

In this work, we have carried out a synthetic survey that describes the impact of measurement design choices on  $X_{\text{CO}_2}$  retrieval performance for shortwave infrared (SWIR) satellite observations. In order to be representative of the wide range of upcoming concept designs, it explored – for a fictitiously varying  $\text{CO}_2\text{M}$ -like instrument – the impact of three different parameters on the measurement: (1) spectral resolution; (2) signal-to-noise ratio (for values spanning 2 orders of magnitude); and (3) spectral band selection. In addition, four exactly defined concepts have been consistently studied: OCO-2,  $\text{CO}_2\text{M}$ , MicroCarb and NanoCarb.

First, the  $X_{\text{CO}_2}$  precision and  $\text{CO}_2$  information content of SWIR measurements improve upon increasing the resolving power and/or the signal-to-noise ratio. For  $\text{CO}_2\text{M}$ -like SNR values, increasing the resolving power by 2.2 orders of magnitude improves the precision by a factor of about 12. For a resolving power of 6000, multiplying the SNR by 100 improves the precision by a factor of about 21. Overall, for these large changes of about 2 orders of magnitude, the precision is found to be more sensitive to SNR improvements than to spectral resolution improvements. However, small-magnitude improvements in resolving power generally yield more  $X_{\text{CO}_2}$  precision improvements than SNR improvements do, especially when  $\text{CO}_2$  spectral lines are resolved. The separate impacts of these two parameters show a broad symmetry in precision as well as in vertical sensitivities: measurements with lower SNR and/or spectral resolution values give more weight to atmospheric layers close to the surface for the retrieved total columns.

The comparison of different spectral band selections included in the SWIR measurement provided two main conclusions. First, including the  $\text{O}_2$   $0.76\ \mu\text{m}$  band strongly increases the information content for parameters that impact the optical path length (for all resolving powers) and helps

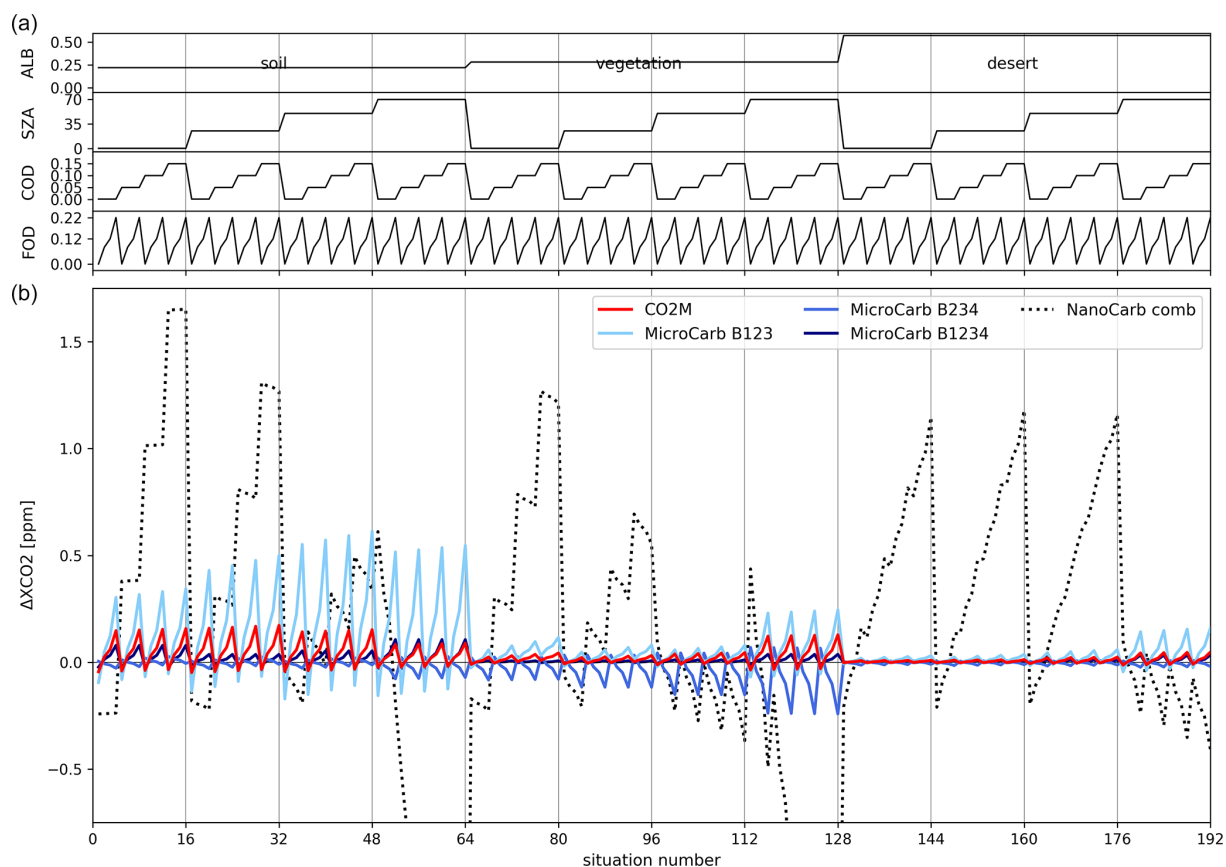


**Figure 11.** Same as Fig. 10, but only results for  $\text{CO}_2\text{M}$ , MicroCarb and NanoCarb are included.

to noticeably reduce the impact of a priori misknowledge of these parameters on retrieved  $X_{\text{CO}_2}$  values. Secondly, the  $\text{CO}_2$   $2.05\ \mu\text{m}$  band (especially for the coarse aerosol mode) carries more information overall than the  $1.6\ \mu\text{m}$  band and thus seems more appropriate for concepts that measure a single  $\text{CO}_2$ -sensitive spectral band, especially at low to mid-level spectral resolution values. These results also highlight how the precise (and accurate to some extent) retrieval of  $X_{\text{CO}_2}$  from SWIR observations relies on the amount of information carried by these observations. Reducing the spectral resolution and/or the number of spectral bands to improve spatial resolution increases errors. If these are constant over a full image, they may be removed when calculating the local enhancements of  $X_{\text{CO}_2}$ . However, they may still hamper absolute  $X_{\text{CO}_2}$  retrievals in plume-free scenes, thus potentially making these observations barely useful for anything but anthropogenic emissions imaging.

The exact  $\text{CO}_2\text{M}$ , MicroCarb and NanoCarb concepts were studied in addition to the fictitiously varying ones. With a spectral resolution that is about 5-times higher but shorter spectral band intervals, MicroCarb shows slightly higher  $\text{CO}_2$  DOFs compared to  $\text{CO}_2\text{M}$ , and its  $X_{\text{CO}_2}$  precision is lower by a factor ranging from about 1.1 to 1.9, depending on the observational situation. Their vertical sen-

sitivities are very similar, and their DOFs for other interfering variables are mostly very close to 1, with the exception of the fine aerosol mode, for which they show slightly lower values. Also, MicroCarb exhibits varying information content on variables related to the optical path length, depending on whether the  $0.76\ \mu\text{m}$  band, the  $1.27\ \mu\text{m}$  band or both of these  $\text{O}_2$ -sensitive bands are included in the calculations. Regarding NanoCarb, which only measures truncated interferograms, not full spectra, its pixel-wise  $X_{\text{CO}_2}$  performance is comparable in many aspects to the performance of low-spectral-resolution and low-SNR spectra-observing concepts. However, the  $X_{\text{CO}_2}$  precision obtained after combining several observations of the same location is close to the  $X_{\text{CO}_2}$  precision of  $\text{CO}_2\text{M}$ . A comparison between NanoCarb DOFs and those of spectra-measuring concepts (regardless of their characteristics) highlights that further improvements of the concept are needed to increase its information content for interfering geophysical variables.

Given its scope, which focused on exploring the impact of concept design parameters on  $X_{\text{CO}_2}$  retrieval performance, this study could not include all the dimensions of a comprehensive mission performance assessment. For example, the accuracy of  $X_{\text{CO}_2}$  retrieval has not been studied, and greater variability in the possible atmospheric conditions (different

aerosol types, layers, contents, thermodynamical profiles,  $\text{CO}_2$  concentration vertical profiles, etc.) could be considered, as is usually done in comprehensive observing system simulation experiments. Also, this work obviously could not explore all possible design parameters (e.g. band-wise variations in spectral sampling ratios, varying wavelength intervals for spectral bands, and combinations of different instruments) that impact  $X_{\text{CO}_2}$  retrieval performance and their implications for anthropogenic plume imaging. These limitations warrant further studies.

This decade will see a large increase in the spaceborne monitoring of  $X_{\text{CO}_2}$  by a wide variety of SWIR-observing concepts. This work enabled us to explore three of the most critical parameters, and it has shown how different we can expect the upcoming  $X_{\text{CO}_2}$  products to be in terms of their respective performance and sensitivities to interfering variables. This hints at the extent of work that will be required to compare, reconcile and cross-calibrate the results produced by so many different satellite concepts, especially if their purpose is to support the independent evaluation of mitigation efforts aiming at Paris Agreement objectives.

*Data availability.* The outputs of radiative transfer simulations and scripts to generate synthetic performance results are available from Matthieu Dogniaux upon request by email (m.dogniaux@sron.nl).

*Supplement.* The supplement related to this article is available online at: <https://doi.org/10.5194/amt-17-5373-2024-supplement>.

*Author contributions.* MD designed this study and carried it out with the help and supervision of CC. MD wrote this article with feedback from CC.

*Competing interests.* The contact author has declared that neither of the authors has any competing interests.

*Disclaimer.* Publisher's note: Copernicus Publications remains neutral with regard to jurisdictional claims made in the text, published maps, institutional affiliations, or any other geographical representation in this paper. While Copernicus Publications makes every effort to include appropriate place names, the final responsibility lies with the authors.

*Acknowledgements.* The authors are thankful for the funding received from Airbus Defence and Space and from CNES and the CNRS, and they are grateful to Raymond Armante and Vincent Cassé for their helpful comments and proofreading of this manuscript.

*Financial support.* Matthieu Dogniaux was funded by Airbus Defence and Space in the framework of a scientific collaboration with École polytechnique. This work has received funding from CNES and CNRS. The Space CARBON Observatory (SCARBO) project, that supported NanoCarb development, received funding from the European Union's H2020 research and innovation program under grant agreement no. 769032.

*Review statement.* This paper was edited by Frank Hase and reviewed by three anonymous referees.

## References

- Ayasse, A. K., Thorpe, A. K., Roberts, D. A., Funk, C. C., Denison, P. E., Frankenberg, C., Steffke, A., and Aubrey, A. D.: Evaluating the effects of surface properties on methane retrievals using a synthetic airborne visible/infrared imaging spectrometer next generation (AVIRIS-NG) image, *Remote Sens. Environ.*, 215, 386–397, <https://doi.org/10.1016/j.rse.2018.06.018>, 2018.
- Baldrige, A. M., Hook, S. J., Grove, C. I., and Rivera, G.: The ASTER spectral library version 2.0, *Remote Sens. Environ.*, 113, 711–715, <https://doi.org/10.1016/j.rse.2008.11.007>, 2009.
- Bertaux, J.-L., Hauchecorne, A., Lefèvre, F., Bréon, F.-M., Blanot, L., Jouglet, D., Lafrique, P., and Akaev, P.: The use of the 1.27  $\mu\text{m}$   $\text{O}_2$  absorption band for greenhouse gas monitoring from space and application to MicroCarb, *Atmos. Meas. Tech.*, 13, 3329–3374, <https://doi.org/10.5194/amt-13-3329-2020>, 2020.
- Boesch, H., Baker, D., Connor, B., Crisp, D., and Miller, C.: Global Characterization of  $\text{CO}_2$  Column Retrievals from Shortwave-Infrared Satellite Observations of the Orbiting Carbon Observatory-2 Mission, *Remote Sens.-Basel*, 3, 270–304, <https://doi.org/10.3390/rs3020270>, 2011.
- Borchardt, J., Gerilowski, K., Krautwurst, S., Bovensmann, H., Thorpe, A. K., Thompson, D. R., Frankenberg, C., Miller, C. E., Duren, R. M., and Burrows, J. P.: Detection and quantification of  $\text{CH}_4$  plumes using the WFM-DOAS retrieval on AVIRIS-NG hyperspectral data, *Atmos. Meas. Tech.*, 14, 1267–1291, <https://doi.org/10.5194/amt-14-1267-2021>, 2021.
- Bovensmann, H., Burrows, J. P., Buchwitz, M., Frerick, J., Noël, S., Rozanov, V. V., Chance, K. V., and Goede, A. P. H.: SCIAMACHY: Mission objectives and measurement modes, *J. Atmos. Sci.*, 56, 127–150, [https://doi.org/10.1175/1520-0469\(1999\)056<0127:SMOAMM>2.0.CO;2](https://doi.org/10.1175/1520-0469(1999)056<0127:SMOAMM>2.0.CO;2), 1999.
- Bovensmann, H., Buchwitz, M., Burrows, J. P., Reuter, M., Krings, T., Gerilowski, K., Schneising, O., Heymann, J., Tretner, A., and Erzinger, J.: A remote sensing technique for global monitoring of power plant  $\text{CO}_2$  emissions from space and related applications, *Atmos. Meas. Tech.*, 3, 781–811, <https://doi.org/10.5194/amt-3-781-2010>, 2010.
- Brooker, L.: CONSTELLATION OF SMALL SATELLITES FOR THE MONITORING OF GREENHOUSE GASES, in: 69th International Astronautical Congress (IAC), Bremen, Germany, 1–5 October 2018.
- Broquet, G., Bréon, F.-M., Renault, E., Buchwitz, M., Reuter, M., Bovensmann, H., Chevallier, F., Wu, L., and Ciais, P.: The potential of satellite spectro-imagery for monitoring  $\text{CO}_2$

- emissions from large cities, *Atmos. Meas. Tech.*, 11, 681–708, <https://doi.org/10.5194/amt-11-681-2018>, 2018.
- Buchwitz, M., de Beek, R., Burrows, J. P., Bovensmann, H., Warneke, T., Notholt, J., Meirink, J. F., Goede, A. P. H., Bergamaschi, P., Körner, S., Heimann, M., and Schulz, A.: Atmospheric methane and carbon dioxide from SCIAMACHY satellite data: initial comparison with chemistry and transport models, *Atmos. Chem. Phys.*, 5, 941–962, <https://doi.org/10.5194/acp-5-941-2005>, 2005.
- Buchwitz, M., Reuter, M., Bovensmann, H., Pillai, D., Heymann, J., Schneising, O., Rozanov, V., Krings, T., Burrows, J. P., Boesch, H., Gerbig, C., Meijer, Y., and Löscher, A.: Carbon Monitoring Satellite (CarbonSat): assessment of atmospheric  $\text{CO}_2$  and  $\text{CH}_4$  retrieval errors by error parameterization, *Atmos. Meas. Tech.*, 6, 3477–3500, <https://doi.org/10.5194/amt-6-3477-2013>, 2013.
- Chedin, A., Scott, N., Wahiche, C., and Moulinier, P.: The Improved Initialization Inversion Method: A High Resolution Physical Method for Temperature Retrievals from Satellites of the TIROS-N Series, *J. Clim. Appl. Meteorol.*, 24, 128–143, [https://doi.org/10.1175/1520-0450\(1985\)024<0128:TIIMA>2.0.CO;2](https://doi.org/10.1175/1520-0450(1985)024<0128:TIIMA>2.0.CO;2), 1985.
- Chevallier, F., Chéruy, F., Scott, N. A., and Chédin, A.: A Neural Network Approach for a Fast and Accurate Computation of a Longwave Radiative Budget, *J. Appl. Meteorol.*, 37, 1385–1397, [https://doi.org/10.1175/1520-0450\(1998\)037<1385:ANNAFA>2.0.CO;2](https://doi.org/10.1175/1520-0450(1998)037<1385:ANNAFA>2.0.CO;2), 1998.
- Chevallier, F., Bréon, F.-M., and Rayner, P. J.: Contribution of the Orbiting Carbon Observatory to the estimation of  $\text{CO}_2$  sources and sinks: Theoretical study in a variational data assimilation framework, *J. Geophys. Res.-Atmos.*, 112, D09307, <https://doi.org/10.1029/2006JD007375>, 2007.
- Chevallier, F., Remaud, M., O'Dell, C. W., Baker, D., Peylin, P., and Cozic, A.: Objective evaluation of surface- and satellite-driven carbon dioxide atmospheric inversions, *Atmos. Chem. Phys.*, 19, 14233–14251, <https://doi.org/10.5194/acp-19-14233-2019>, 2019.
- Ciais, P., Rayner, P., Chevallier, F., Bousquet, P., Logan, M., Peylin, P., and Ramonet, M.: Atmospheric inversions for estimating  $\text{CO}_2$  fluxes: methods and perspectives, *Climatic Change*, 103, 69–92, <https://doi.org/10.1007/s10584-010-9909-3>, 2010.
- Connor, B. J., Boesch, H., Toon, G., Sen, B., Miller, C., and Crisp, D.: Orbiting Carbon Observatory: Inverse method and prospective error analysis, *J. Geophys. Res.-Atmos.*, 113, D05305, <https://doi.org/10.1029/2006JD008336>, 2008.
- Crisp, D., Pollock, H. R., Rosenberg, R., Chapsky, L., Lee, R. A. M., Oyafuso, F. A., Frankenberg, C., O'Dell, C. W., Bruegge, C. J., Doran, G. B., Eldering, A., Fisher, B. M., Fu, D., Gunson, M. R., Mandrake, L., Osterman, G. B., Schwandner, F. M., Sun, K., Taylor, T. E., Wennberg, P. O., and Wunch, D.: The on-orbit performance of the Orbiting Carbon Observatory-2 (OCO-2) instrument and its radiometrically calibrated products, *Atmos. Meas. Tech.*, 10, 59–81, <https://doi.org/10.5194/amt-10-59-2017>, 2017.
- Cusworth, D. H., Duren, R. M., Thorpe, A. K., Eastwood, M. L., Green, R. O., Dennison, P. E., Frankenberg, C., Heckler, J. W., Asner, G. P., and Miller, C. E.: Quantifying Global Power Plant Carbon Dioxide Emissions With Imaging Spectroscopy, *AGU Adv.*, 2, e2020AV000350, <https://doi.org/10.1029/2020AV000350>, 2021.
- Dogniaux, M., Crevoisier, C., Armante, R., Capelle, V., Delahaye, T., Cassé, V., De Mazière, M., Deutscher, N. M., Feist, D. G., Garcia, O. E., Griffith, D. W. T., Hase, F., Iraci, L. T., Kivi, R., Morino, I., Notholt, J., Pollard, D. F., Roehl, C. M., Shiomi, K., Strong, K., Té, Y., Velazco, V. A., and Warneke, T.: The Adaptable 4A Inversion (SAI): description and first  $X_{\text{CO}_2}$  retrievals from Orbiting Carbon Observatory-2 (OCO-2) observations, *Atmos. Meas. Tech.*, 14, 4689–4706, <https://doi.org/10.5194/amt-14-4689-2021>, 2021.
- Dogniaux, M., Crevoisier, C., Gousset, S., Le Coarer, É., Ferrec, Y., Croizé, L., Wu, L., Hasekamp, O., Sic, B., and Brooker, L.: The Space Carbon Observatory (SCARBO) concept: assessment of  $X_{\text{CO}_2}$  and  $X_{\text{CH}_4}$  retrieval performance, *Atmos. Meas. Tech.*, 15, 4835–4858, <https://doi.org/10.5194/amt-15-4835-2022>, 2022.
- Duren, R. M. and Miller, C. E.: Measuring the carbon emissions of megacities, *Nat. Clim. Change*, 2, 560–562, <https://doi.org/10.1038/nclimate1629>, 2012.
- Eldering, A., O'Dell, C. W., Wennberg, P. O., Crisp, D., Gunson, M. R., Viatte, C., Avis, C., Braverman, A., Castano, R., Chang, A., Chapsky, L., Cheng, C., Connor, B., Dang, L., Doran, G., Fisher, B., Frankenberg, C., Fu, D., Granat, R., Hobbs, J., Lee, R. A. M., Mandrake, L., McDuffie, J., Miller, C. E., Myers, V., Natraj, V., O'Brien, D., Osterman, G. B., Oyafuso, F., Payne, V. H., Pollock, H. R., Polonsky, I., Roehl, C. M., Rosenberg, R., Schwandner, F., Smyth, M., Tang, V., Taylor, T. E., To, C., Wunch, D., and Yoshimizu, J.: The Orbiting Carbon Observatory-2: first 18 months of science data products, *Atmos. Meas. Tech.*, 10, 549–563, <https://doi.org/10.5194/amt-10-549-2017>, 2017.
- Friedlingstein, P., O'Sullivan, M., Jones, M. W., Andrew, R. M., Gregor, L., Hauck, J., Le Quéré, C., Luijkx, I. T., Olsen, A., Peters, G. P., Peters, W., Pongratz, J., Schwingshackl, C., Sitch, S., Canadell, J. G., Ciais, P., Jackson, R. B., Alin, S. R., Alkama, R., Arneth, A., Arora, V. K., Bates, N. R., Becker, M., Bellouin, N., Bittig, H. C., Bopp, L., Chevallier, F., Chini, L. P., Cronin, M., Evans, W., Falk, S., Feely, R. A., Gasser, T., Gehlen, M., Gkritzalis, T., Gloege, L., Grassi, G., Gruber, N., Gürses, Ö., Harris, I., Hefner, M., Houghton, R. A., Hurtt, G. C., Iida, Y., Ilyina, T., Jain, A. K., Jersild, A., Kadono, K., Kato, E., Kennedy, D., Klein Goldewijk, K., Knauer, J., Korsbakken, J. I., Landschützer, P., Lefèvre, N., Lindsay, K., Liu, J., Liu, Z., Marland, G., Mayot, N., McGrath, M. J., Metzl, N., Monacchi, N. M., Munro, D. R., Nakaoka, S.-I., Niwa, Y., O'Brien, K., Ono, T., Palmer, P. I., Pan, N., Pierrot, D., Pockock, K., Poulter, B., Resplandy, L., Robertson, E., Rödenbeck, C., Rodriguez, C., Rosan, T. M., Schwinger, J., Séférian, R., Shutler, J. D., Skjelvan, I., Steinhoff, T., Sun, Q., Sutton, A. J., Sweeney, C., Takao, S., Tanhua, T., Tans, P. P., Tian, X., Tian, H., Tilbrook, B., Tsujino, H., Tubiello, F., van der Werf, G. R., Walker, A. P., Wanninkhof, R., Whitehead, C., Willstrand Wranne, A., Wright, R., Yuan, W., Yue, C., Yue, X., Zaehle, S., Zeng, J., and Zheng, B.: Global Carbon Budget 2022, *Earth Syst. Sci. Data*, 14, 4811–4900, <https://doi.org/10.5194/essd-14-4811-2022>, 2022.
- Galli, A., Guerlet, S., Butz, A., Aben, I., Suto, H., Kuze, A., Deutscher, N. M., Notholt, J., Wunch, D., Wennberg, P. O., Griffith, D. W. T., Hasekamp, O., and Landgraf, J.: The impact of spectral resolution on satellite retrieval accuracy of  $\text{CO}_2$  and  $\text{CH}_4$ , *Atmos. Meas. Tech.*, 7, 1105–1119, <https://doi.org/10.5194/amt-7-1105-2014>, 2014.

- Gousset, S., Croizé, L., Le Coarer, E., Ferrec, Y., Rodrigo-Rodrigo, J., Brooker, L., and consortium, for the S.: NanoCarb hyperspectral sensor: on performance optimization and analysis for greenhouse gas monitoring from a constellation of small satellites, *CEAS Space J.*, 11, 507–524, <https://doi.org/10.1007/s12567-019-00273-9>, 2019.
- Hamlin, L., Green, R. O., Mouroulis, P., Eastwood, M., Wilson, D., Dudik, M., and Paine, C.: Imaging spectrometer science measurements for Terrestrial Ecology: AVIRIS and new developments, in: 2011 Aerospace Conference, Big Sky, MT, USA, 5–12 March 2011, IEEE, 1–7, <https://doi.org/10.1109/AERO.2011.5747395>, 2011.
- Hess, M., Koepke, P., and Schult, I.: Optical Properties of Aerosols and Clouds: The Software Package OPAC, *B. Am. Meteorol. Soc.*, 79, 831–844, [https://doi.org/10.1175/1520-0477\(1998\)079<0831:OPOAAC>2.0.CO;2](https://doi.org/10.1175/1520-0477(1998)079<0831:OPOAAC>2.0.CO;2), 1998.
- Houweling, S., Hartmann, W., Aben, I., Schrijver, H., Skidmore, J., Roelofs, G.-J., and Breon, F.-M.: Evidence of systematic errors in SCIAMACHY-observed CO<sub>2</sub> due to aerosols, *Atmos. Chem. Phys.*, 5, 3003–3013, <https://doi.org/10.5194/acp-5-3003-2005>, 2005.
- Inoue, M., Morino, I., Uchino, O., Nakatsuru, T., Yoshida, Y., Yokota, T., Wunch, D., Wennberg, P. O., Roehl, C. M., Griffith, D. W. T., Velazco, V. A., Deutscher, N. M., Warneke, T., Notholt, J., Robinson, J., Sherlock, V., Hase, F., Blumenstock, T., Rettinger, M., Sussmann, R., Kyrö, E., Kivi, R., Shiomi, K., Kawakami, S., De Mazière, M., Arnold, S. G., Feist, D. G., Barrow, E. A., Barney, J., Dubey, M., Schneider, M., Iraci, L. T., Podolske, J. R., Hillyard, P. W., Machida, T., Sawa, Y., Tsuboi, K., Matsueda, H., Sweeney, C., Tans, P. P., Andrews, A. E., Biraud, S. C., Fukuyama, Y., Pittman, J. V., Kort, E. A., and Tanaka, T.: Bias corrections of GOSAT SWIR XCO<sub>2</sub> and XCH<sub>4</sub> with TC-CON data and their evaluation using aircraft measurement data, *Atmos. Meas. Tech.*, 9, 3491–3512, <https://doi.org/10.5194/amt-9-3491-2016>, 2016.
- IPCC: Summary for Policymakers, in: *Clim. Change 2021 Phys. Sci. Basis Contrib. Work. Group Sixth Assess. Rep. Intergov. Panel Clim. Change*, edited by: Masson-Delmotte, V., Zhai, P., Pirani, A., Connors, S. L., Péan, C., Berger, S., Caud, N., Chen, Y., Goldfarb, L., Gomis, M. I., Huang, M., Leitzell, K., Lonnoy, E., Matthews, J. B. R., Maycock, T. K., Waterfield, T., Yelekçi, O., Yu, R., and Zhou, B., IPCC, <https://doi.org/10.1017/9781009157896.001>, 2021.
- Jacquinet-Husson, N., Armante, R., Scott, N. A., Chédin, A., Crépeau, L., Boutammene, C., Bouhdaoui, A., Crevoisier, C., Capelle, V., Boone, C., Poulet-Crovisier, N., Barbe, A., Benner, D. [Chris, Boudon, V., Brown, L. R., Buldyreva, J., Campargue, A., Coudert, L. H., Devi, V. M., Down, M. J., Drouin, B. J., Fayt, A., Fittschen, C., Flaud, J.-M., Gamache, R. R., Harrison, J. J., Hill, C., Hodnebrog, Ø., Hu, S.-M., Jacquemart, D., Jolly, A., Jiménez, E., Lavrentieva, N. N., Liu, A.-W., Lodi, L., Lyulin, O. M., Massie, S. T., Mikhailenko, S., Müller, H. S. P., Naumenko, O. V., Nikitin, A., Nielsen, C. J., Orphal, J., Perevalov, V. I., Perrin, A., Polovtseva, E., Predoi-Cross, A., Rotger, M., Ruth, A. A., Yu, S. S., Sung, K., Tashkun, S. A., Tennyson, J., Tyuterev, V. I., G., Auwera, J. [Vander, Voronin, B. A., and Makie, A.: The 2015 edition of the GEISA spectroscopic database, *J. Mol. Spectrosc.*, 327, 31–72, <https://doi.org/10.1016/j.jms.2016.06.007>, 2016.
- Janssens-Maenhout, G., Pinty, B., Dowell, M., Zunker, H., Andersson, E., Balsamo, G., Bézy, J.-L., Brunhes, T., Bösch, H., Bockov, B., Brunner, D., Buchwitz, M., Crisp, D., Ciais, P., Counet, P., Dee, D., van der Gon, H. D., Dolman, H., Drinkwater, M. R., Dubovik, O., Engelen, R., Fehr, T., Fernandez, V., Heimann, M., Holmlund, K., Houweling, S., Husband, R., Juvyns, O., Kentarchos, A., Landgraf, J., Lang, R., Löscher, A., Marshall, J., Meijer, Y., Nakajima, M., Palmer, P. I., Peylin, P., Rayner, P., Scholze, M., Sierk, B., Tamminen, J., and Veeffkind, P.: Toward an Operational Anthropogenic CO<sub>2</sub> Emissions Monitoring and Verification Support Capacity, *B. Am. Meteorol. Soc.*, 101, E1439–E1451, <https://doi.org/10.1175/BAMS-D-19-0017.1>, 2020.
- Krings, T., Gerilowski, K., Buchwitz, M., Reuter, M., Tretner, A., Erzinger, J., Heinze, D., Pflüger, U., Burrows, J. P., and Bovensmann, H.: MAMAP – a new spectrometer system for column-averaged methane and carbon dioxide observations from aircraft: retrieval algorithm and first inversions for point source emission rates, *Atmos. Meas. Tech.*, 4, 1735–1758, <https://doi.org/10.5194/amt-4-1735-2011>, 2011.
- Kuhlmann, G., Broquet, G., Marshall, J., Clément, V., Löscher, A., Meijer, Y., and Brunner, D.: Detectability of CO<sub>2</sub> emission plumes of cities and power plants with the Copernicus Anthropogenic CO<sub>2</sub> Monitoring (CO2M) mission, *Atmos. Meas. Tech.*, 12, 6695–6719, <https://doi.org/10.5194/amt-12-6695-2019>, 2019.
- Lamouroux, J., Régalia, L., Thomas, X., Vander Auwera, J., Gamache, R. R., and Hartmann, J.-M.: CO<sub>2</sub> line-mixing database and software update and its tests in the 2.1 μm and 4.3 μm regions, *J. Quant. Spectrosc. Ra.*, 151, 88–96, <https://doi.org/10.1016/j.jqsrt.2014.09.017>, 2015.
- Liou, K.-Nan.: An introduction to atmospheric radiation [electronic resource], 2nd edn., Academic Press, Amsterdam, ISBN: 9780124514515, 2002.
- Liu, X., Huang, Y., Xu, X., Li, X., Li, X., Ciais, P., Lin, P., Gong, K., Ziegler, A. D., Chen, A., Gong, P., Chen, J., Hu, G., Chen, Y., Wang, S., Wu, Q., Huang, K., Estes, L., and Zeng, Z.: High-spatiotemporal-resolution mapping of global urban change from 1985 to 2015, *Nat. Sustain.*, 3, 564–570, <https://doi.org/10.1038/s41893-020-0521-x>, 2020.
- Lwasa, S., Seto, K. C., Bai, X., Blanco, H., Gurney, K. R., Kilkış, S., Lucon, O., Murakami, J., Pan, J., Sharifi, A., and Yamagata, Y.: Urban systems and other settlements, in: IPCC, 2022: Climate Change 2022: Mitigation of Climate Change. Contribution of Working Group III to the Sixth Assessment Report of the Intergovernmental Panel on Climate Change, edited by: Shukla, P. R., Skea, J., Slade, R., Kouradajie, A. Al, van Diemen, R., McCollum, D., Pathak, M., Some, S., Vyas, P., Fradera, R., Belkacemi, M., Hasija, A., Lisboa, G., Luz, S., and Malley, J., Cambridge University Press, Cambridge, UK and New York, NY, USA, <https://doi.org/10.1017/9781009157926.010>, 2022.
- Matsunaga, T. and Tanimoto, H.: Greenhouse gas observation by TANSO-3 onboard GOSAT-GW, in: *Sensors, Systems, and Next-Generation Satellites XXVI*, Berlin, Germany, 5–8 September 2022, SPIE, 122640B, <https://doi.org/10.1117/12.2639221>, 2022.
- Meijer, Y. and Earth and Mission Science Division: Copernicus CO<sub>2</sub> Monitoring Mission Requirements Document, [https://esamultimedia.esa.int/docs/EarthObservation/CO2M\\_](https://esamultimedia.esa.int/docs/EarthObservation/CO2M_)

- MRD\_v2.0\_Issued20190927.pdf (last access: 18 August 2024), 2020.
- Nassar, R., Mastrogiacomo, J.-P., Bateman-Hemphill, W., McCracken, C., MacDonald, C. G., Hill, T., O'Dell, C. W., Kiel, M., and Crisp, D.: Advances in quantifying power plant CO<sub>2</sub> emissions with OCO-2, *Remote Sens. Environ.*, 264, 112579, <https://doi.org/10.1016/j.rse.2021.112579>, 2021.
- Noël, S., Reuter, M., Buchwitz, M., Borchardt, J., Hilker, M., Bovensmann, H., Burrows, J. P., Di Noia, A., Suto, H., Yoshida, Y., Buschmann, M., Deutscher, N. M., Feist, D. G., Griffith, D. W. T., Hase, F., Kivi, R., Morino, I., Notholt, J., Ohyama, H., Petri, C., Podolske, J. R., Pollard, D. F., Sha, M. K., Shiomi, K., Sussmann, R., Té, Y., Velazco, V. A., and Warneke, T.: XCO<sub>2</sub> retrieval for GOSAT and GOSAT-2 based on the FOCAL algorithm, *Atmos. Meas. Tech.*, 14, 3837–3869, <https://doi.org/10.5194/amt-14-3837-2021>, 2021.
- O'Dell, C. W., Eldering, A., Wennberg, P. O., Crisp, D., Gunson, M. R., Fisher, B., Frankenberg, C., Kiel, M., Lindqvist, H., Mandrake, L., Merrelli, A., Natraj, V., Nelson, R. R., Osterman, G. B., Payne, V. H., Taylor, T. E., Wunch, D., Drouin, B. J., Oyafuso, F., Chang, A., McDuffie, J., Smyth, M., Baker, D. F., Basu, S., Chevallier, F., Crowell, S. M. R., Feng, L., Palmer, P. I., Dubey, M., García, O. E., Griffith, D. W. T., Hase, F., Iraci, L. T., Kivi, R., Morino, I., Notholt, J., Ohyama, H., Petri, C., Roehl, C. M., Sha, M. K., Strong, K., Sussmann, R., Te, Y., Uchino, O., and Velazco, V. A.: Improved retrievals of carbon dioxide from Orbiting Carbon Observatory-2 with the version 8 ACOS algorithm, *Atmos. Meas. Tech.*, 11, 6539–6576, <https://doi.org/10.5194/amt-11-6539-2018>, 2018.
- Papayannis, A., Amiridis, V., Mona, L., Tsaknakis, G., Balis, D., Bösenberg, J., Chaikovski, A., De Tomasi, F., Grigorov, I., Mattis, I., Mitev, V., Müller, D., Nickovic, S., Pérez, C., Pietruczuk, A., Pisani, G., Ravetta, F., Rizi, V., Sicard, M., Trickl, T., Wiegner, M., Gerding, M., Mamouri, R. E., D'Amico, G., and Pappalardo, G.: Systematic lidar observations of Saharan dust over Europe in the frame of EARLINET (2000–2002), *J. Geophys. Res.-Atmos.*, 113, D10204, <https://doi.org/10.1029/2007JD009028>, 2008.
- Pascal, V., Buil, C., Loesel, J., Tazuide, L., Jouglet, D., and Buisson, F.: An improved microcarb dispersive instrumental concept for the measurement of greenhouse gases concentration in the atmosphere, in: International Conference on Space Optics — ICSSO 2014, Tenerife, Canary Islands, Spain, 6–10 October 2014, SPIE, 1028–1036, <https://doi.org/10.1117/12.2304219>, 2017.
- Peiro, H., Crowell, S., Schuh, A., Baker, D. F., O'Dell, C., Jacobson, A. R., Chevallier, F., Liu, J., Eldering, A., Crisp, D., Deng, F., Weir, B., Basu, S., Johnson, M. S., Philip, S., and Baker, I.: Four years of global carbon cycle observed from the Orbiting Carbon Observatory 2 (OCO-2) version 9 and in situ data and comparison to OCO-2 version 7, *Atmos. Chem. Phys.*, 22, 1097–1130, <https://doi.org/10.5194/acp-22-1097-2022>, 2022.
- Pillai, D., Buchwitz, M., Gerbig, C., Koch, T., Reuter, M., Bovensmann, H., Marshall, J., and Burrows, J. P.: Tracking city CO<sub>2</sub> emissions from space using a high-resolution inverse modelling approach: a case study for Berlin, Germany, *Atmos. Chem. Phys.*, 16, 9591–9610, <https://doi.org/10.5194/acp-16-9591-2016>, 2016.
- Rayner, P. J. and O'Brien, D. M.: The utility of remotely sensed CO<sub>2</sub> concentration data in surface source inversions, *Geophys. Res. Lett.*, 28, 175–178, <https://doi.org/10.1029/2000GL011912>, 2001.
- Reuter, M., Buchwitz, M., Schneising, O., Heymann, J., Bovensmann, H., and Burrows, J. P.: A method for improved SCIAMACHY CO<sub>2</sub> retrieval in the presence of optically thin clouds, *Atmos. Meas. Tech.*, 3, 209–232, <https://doi.org/10.5194/amt-3-209-2010>, 2010.
- Reuter, M., Buchwitz, M., Schneising, O., Krautwurst, S., O'Dell, C. W., Richter, A., Bovensmann, H., and Burrows, J. P.: Towards monitoring localized CO<sub>2</sub> emissions from space: co-located regional CO<sub>2</sub> and NO<sub>2</sub> enhancements observed by the OCO-2 and S5P satellites, *Atmos. Chem. Phys.*, 19, 9371–9383, <https://doi.org/10.5194/acp-19-9371-2019>, 2019.
- Roche, S., Strong, K., Wunch, D., Mendonca, J., Sweeney, C., Baier, B., Biraud, S. C., Laughner, J. L., Toon, G. C., and Connor, B. J.: Retrieval of atmospheric CO<sub>2</sub> vertical profiles from ground-based near-infrared spectra, *Atmos. Meas. Tech.*, 14, 3087–3118, <https://doi.org/10.5194/amt-14-3087-2021>, 2021.
- Rodgers, C. D.: *Inverse Methods for Atmospheric Sounding*, World Scientific, <https://doi.org/10.1142/3171>, 2000.
- Rusli, S. P., Hasekamp, O., van de Brugh, J., Fu, G., Meijer, Y., and Landgraf, J.: Anthropogenic CO<sub>2</sub> monitoring satellite mission: the need for multi-angle polarimetric observations, *Atmos. Meas. Tech.*, 14, 1167–1190, <https://doi.org/10.5194/amt-14-1167-2021>, 2021.
- Scott, N. A. and Chédin, A.: A Fast Line-by-Line Method for Atmospheric Absorption Computations: The Automated Atmospheric Absorption Atlas, *J. Appl. Meteorol.*, 20, 802–812, 1981.
- Spurr, R. J. D.: Simultaneous derivation of intensities and weighting functions in a general pseudo-spherical discrete ordinate radiative transfer treatment, *J. Quant. Spectrosc. Ra.*, 75, 129–175, [https://doi.org/10.1016/S0022-4073\(01\)00245-X](https://doi.org/10.1016/S0022-4073(01)00245-X), 2002.
- Strandgren, J., Krutz, D., Wilzewski, J., Paproth, C., Sebastian, I., Gurney, K. R., Liang, J., Roiger, A., and Butz, A.: Towards spaceborne monitoring of localized CO<sub>2</sub> emissions: an instrument concept and first performance assessment, *Atmos. Meas. Tech.*, 13, 2887–2904, <https://doi.org/10.5194/amt-13-2887-2020>, 2020.
- Taylor, T. E., O'Dell, C. W., Crisp, D., Kuze, A., Lindqvist, H., Wennberg, P. O., Chatterjee, A., Gunson, M., Eldering, A., Fisher, B., Kiel, M., Nelson, R. R., Merrelli, A., Osterman, G., Chevallier, F., Palmer, P. I., Feng, L., Deutscher, N. M., Dubey, M. K., Feist, D. G., García, O. E., Griffith, D. W. T., Hase, F., Iraci, L. T., Kivi, R., Liu, C., De Mazière, M., Morino, I., Notholt, J., Oh, Y.-S., Ohyama, H., Pollard, D. F., Rettinger, M., Schneider, M., Roehl, C. M., Sha, M. K., Shiomi, K., Strong, K., Sussmann, R., Té, Y., Velazco, V. A., Vrekoussis, M., Warneke, T., and Wunch, D.: An 11-year record of XCO<sub>2</sub> estimates derived from GOSAT measurements using the NASA ACOS version 9 retrieval algorithm, *Earth Syst. Sci. Data*, 14, 325–360, <https://doi.org/10.5194/essd-14-325-2022>, 2022.
- Taylor, T. E., O'Dell, C. W., Baker, D., Bruegge, C., Chang, A., Chapsky, L., Chatterjee, A., Cheng, C., Chevallier, F., Crisp, D., Dang, L., Drouin, B., Eldering, A., Feng, L., Fisher, B., Fu, D., Gunson, M., Haemmerle, V., Keller, G. R., Kiel, M., Kuai, L., Kurosu, T., Lambert, A., Laughner, J., Lee, R., Liu, J., Mandrake, L., Marchetti, Y., McGarragh, G., Merrelli, A., Nelson, R. R., Osterman, G., Oyafuso, F., Palmer, P. I., Payne, V. H., Rosenberg, R., Somkuti, P., Spiers, G., To, C., Weir, B., Wennberg, P. O.,

- Yu, S., and Zong, J.: Evaluating the consistency between OCO-2 and OCO-3 XCO<sub>2</sub> estimates derived from the NASA ACOS version 10 retrieval algorithm, *Atmos. Meas. Tech.*, 16, 3173–3209, <https://doi.org/10.5194/amt-16-3173-2023>, 2023.
- Tran, H. and Hartmann, J.-M.: An improved O<sub>2</sub> A band absorption model and its consequences for retrievals of photon paths and surface pressures, *J. Geophys. Res.-Atmos.*, 113, D18104, <https://doi.org/10.1029/2008JD010011>, 2008.
- Varon, D. J., Jacob, D. J., McKeever, J., Jervis, D., Durak, B. O. A., Xia, Y., and Huang, Y.: Quantifying methane point sources from fine-scale satellite observations of atmospheric methane plumes, *Atmos. Meas. Tech.*, 11, 5673–5686, <https://doi.org/10.5194/amt-11-5673-2018>, 2018.
- Wilzewski, J. S., Roiger, A., Strandgren, J., Landgraf, J., Feist, D. G., Velazco, V. A., Deutscher, N. M., Morino, I., Ohyama, H., Té, Y., Kivi, R., Warneke, T., Notholt, J., Dubey, M., Sussmann, R., Rettinger, M., Hase, F., Shiomi, K., and Butz, A.: Spectral sizing of a coarse-spectral-resolution satellite sensor for XCO<sub>2</sub>, *Atmos. Meas. Tech.*, 13, 731–745, <https://doi.org/10.5194/amt-13-731-2020>, 2020.
- Wu, L., Hasekamp, O., Hu, H., aan de Brugh, J., Landgraf, J., Butz, A., and Aben, I.: Full-physics carbon dioxide retrievals from the Orbiting Carbon Observatory-2 (OCO-2) satellite by only using the 2.06 μm band, *Atmos. Meas. Tech.*, 12, 6049–6058, <https://doi.org/10.5194/amt-12-6049-2019>, 2019.
- Wu, L., aan de Brugh, J., Meijer, Y., Sierk, B., Hasekamp, O., Butz, A., and Landgraf, J.: XCO<sub>2</sub> observations using satellite measurements with moderate spectral resolution: investigation using GOSAT and OCO-2 measurements, *Atmos. Meas. Tech.*, 13, 713–729, <https://doi.org/10.5194/amt-13-713-2020>, 2020.
- Yang, D., Boesch, H., Liu, Y., Somkuti, P., Cai, Z., Chen, X., Di Noia, A., Lin, C., Lu, N., Lyu, D., Parker, R. J., Tian, L., Wang, M., Webb, A., Yao, L., Yin, Z., Zheng, Y., Deutscher, N. M., Griffith, D. W. T., Hase, F., Kivi, R., Morino, I., Notholt, J., Ohyama, H., Pollard, D. F., Shiomi, K., Sussmann, R., Té, Y., Velazco, V. A., Warneke, T., and Wunch, D.: Toward High Precision XCO<sub>2</sub> Retrievals From TanSat Observations: Retrieval Improvement and Validation Against TCCON Measurements, *J. Geophys. Res.-Atmos.*, 125, e2020JD032794, <https://doi.org/10.1029/2020JD032794>, 2020.
- Zheng, B., Chevallier, F., Ciais, P., Broquet, G., Wang, Y., Lian, J., and Zhao, Y.: Observing carbon dioxide emissions over China's cities and industrial areas with the Orbiting Carbon Observatory-2, *Atmos. Chem. Phys.*, 20, 8501–8510, <https://doi.org/10.5194/acp-20-8501-2020>, 2020.